

An NGA Model for the Average Horizontal Component of Peak Ground Motion and Response Spectra

Brian S.-J. Chiou^{a)} and Robert R. Youngs, ^{b)} M.EERI

We present a model for estimating horizontal ground motion amplitudes caused by shallow crustal earthquakes occurring in active tectonic environments. The model provides predictive relationships for the orientation-independent average horizontal component of ground motions. Relationships are provided for peak acceleration, peak velocity, and 5-percent damped pseudo-spectral acceleration for spectral periods of 0.01 to 10 seconds. The model represents an update of the relationships developed by Sadigh et al. (1997) and incorporates improved magnitude and distance scaling forms as well as hanging-wall effects. Site effects are represented by smooth functions of average shear wave velocity of the upper 30 m (V_{s30}) and sediment depth. The new model predicts median ground motion that is similar to Sadigh et al. (1997) at short spectral period, but lower ground motions at longer periods. The new model produces slightly lower ground motions in the distance range of 10 to 50 km and larger ground motions at larger distances. The aleatory variability in ground motion amplitude was found to depend upon earthquake magnitude and on the degree of nonlinear soil response. For large magnitude earthquakes, the aleatory variability is larger than found by Sadigh et al. (1997). [DOI: 10.1193/1.2894832]

INTRODUCTION

This paper presents a ground motion model developed as part of the Pacific Earthquake Engineering Research Center's (PEER) Next Generation Attenuation model (NGA) project. The model is based on analyses of the PEER-NGA empirical strong-motion database (Chiou et al. 2008). We consider the model presented here to be an update of the set of models developed by Sadigh et al. (1997). As such, we have systematically reviewed the various aspects of the model (e.g., magnitude and distance scaling, site effects, style of faulting effect) and have introduced modifications to the formulation of Sadigh et al. (1997) to incorporate the results of both analyses of empirical data and numerical modeling of earthquake ground motions.

In the following, we first describe the selection of the empirical data used to develop the model. We then describe the development of the ground-motion model formulation, followed by a brief description of the process used to define the model coefficients. Finally, we compare the model predictions with those obtained using Sadigh et al. (1997).

^{a)} Division of Research and Innovation, California Department of Transportation, Sacramento, CA

^{b)} Geomatrix consultants, Inc., 2101 Webster St., 12th Floor, Oakland, CA 94612

STRONG MOTION DATABASE

DATA SELECTION

The empirical database used in this study was derived from the PEER-NGA empirical strong-motion database that contains 3,551 recordings from 173 earthquakes. Our ground motion model was developed to represent free-field motions from shallow crustal earthquakes in active tectonic regions, principally California. Data from earthquakes that occurred in oceanic crust offshore of California and Taiwan were excluded because ground motions from these types of events have been found to be more consistent with ground motions from Wadati-Benioff zone (subduction intraslab) earthquakes than shallow crustal earthquakes (Geomatrix Consultants 1995). Data from the 1992 Cape Mendocino earthquakes were included because the source depth places the event above the likely interface location (Oppenheimer et al. 1993). Four 1997 northwest China earthquakes were excluded because of their large depths (≥ 20 km) and the very limited information about the events and their recordings. Data from the 1979 St Elias earthquake were excluded because we interpret this earthquake to have occurred on a subduction zone interface based on its depth, dip, and location. Data from the 1985 Nahanni and 1992 Roermond, Netherlands earthquakes were included as these earthquakes are interpreted to have occurred at the boundary of stable continental regions (SCR) with active tectonic regions.

The remaining earthquakes are from a variety of active tectonic regions. We start with the hypothesis that the ground motions from these separate active tectonic regions are similar and examine this hypothesis during model development. We include data from aftershocks allowing for the systematic differences in the ground motion amplitudes produced by main shocks and aftershocks. Our reason for including the aftershock data is that they provide additional information to constrain the site model coefficients.

Recordings made in large buildings and at depth were removed, eliminating several additional earthquakes, notably the 1935 Helena, Montana and several Imperial Valley, California earthquakes recorded at the old Imperial Valley Irrigation District site. We included records from sites that have been characterized as having topographic effects (e.g., Tarzana Cedar Hill Nursery, Pacoima Dam left abutment). Our rationale for including these records is that the effect of topography has not been systematically studied for all of the records in the database and many other recording stations may have topographic enhancement or suppression of ground motions. Topographic effects are considered to be part of the variability introduced into ground motions by travel path and site effects.

The ground motion measure used in this model is the orientation-independent ground motion measure GMRot150 defined by Boore et al. (2006). Use of this ground motion measure eliminates recordings for which only a single horizontal component was obtained, notably the Cholame-Shandon Array #2 recording from the 1966 Parkfield earthquake.

As discussed later in the paper, we limit the data to recordings within 70 km of the earthquake rupture in order to remove the effects of bias in the strong motion data

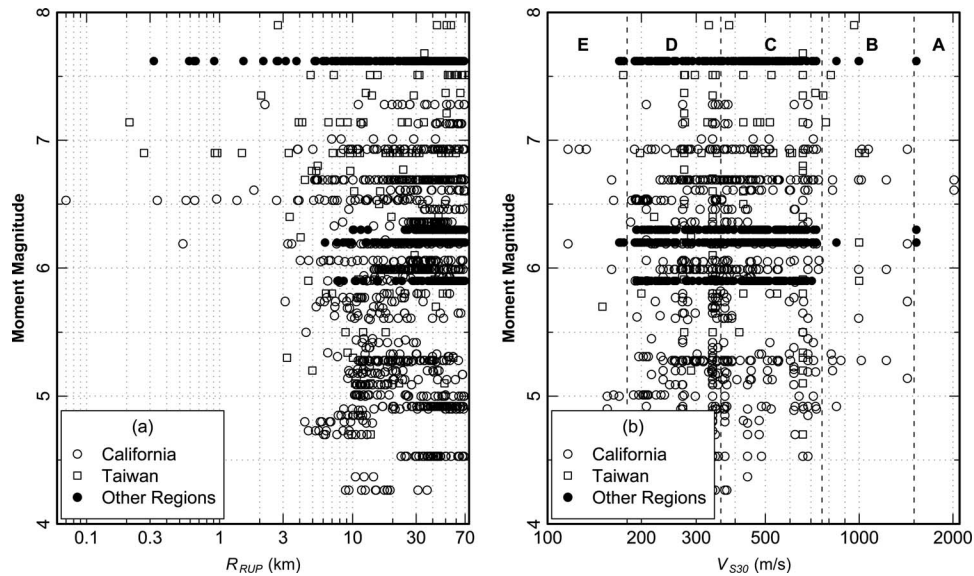


Figure 1. (a) Magnitude-distance-region distribution of selected recordings. (b) V_{S30} -magnitude-region distribution of selected recordings. V_{S30} ranges for NEHRP site classes are indicated by the vertical dashed lines.

sample. This limitation results in a total data set of 1950 recordings from 125 earthquakes. Figure 1 shows the distribution of the selected data in terms of magnitude, distance, and the average shear wave velocity of the upper 30 m (V_{S30}). The earthquakes and recordings used in the analysis are tabulated in Chiou and Youngs (2008).

SUPPLEMENTING PEER-NGA METADATA

The PEER-NGA database does not contain the full set of metadata for many of the recordings selected for use in developing our ground motion model. The missing values were imputed (estimated) as follows: Missing values of the strike, dip, rake, and/or depth to top of rupture were estimated from other associated events such as the mainshock or other aftershocks, or from the tectonic environment. For those earthquakes unassociated with other events, fault dips were assigned based on known or inferred mechanisms as follows: 90° for strike-slip, 40° for reverse (based on the average value reported by Sibson and Xie 1998), and 55° for normal (generic value for normal faults and close to the average of 54° for the normal mechanisms with known dips in the PEER-NGA database). Values of rupture distance, R_{RUP} , Joyner-Boore distance, R_{JB} , and the source-site angle θ_{SITE} were estimated by selecting the median values from 101 simulations of earthquake ruptures using the earthquake size and known or inferred information on the hypocentral depth, fault strike, fault dip, and rupture mechanism (Chiou and Youngs 2008).

The thickness of the near-surface sediments is represented in our model by the depth to a shear wave velocity of 1.0 km/s, $Z_{1.0}$. These data are available in the PEER-NGA database for sites within the Southern California Earthquake Center 3-D basin model (Magistrale et al. 2000), for sites in the USGS velocity model for the San Francisco Bay area (Boatwright et al. 2004), for sites in the Eel River basin (Graves 1994), and for sites where measured velocities reach this velocity horizon. Note that in our study we updated the $Z_{1.0}$ values from SCEC-3D Version 2 to those from Version 4. For the remaining sites $Z_{1.0}$ was estimated through the following correlation with V_{S30} developed from the data in the PEER-NGA database:

$$\ln(Z_{1.0}) = 28.5 - \frac{3.82}{8} \ln(V_{S30}^8 + 378.7^8) \quad (1)$$

SUPPLEMENTAL EMPIRICAL DATA

The PEER-NGA strong motion data were supplemented with ground motion data from the California TriNet system. Time histories recorded at broad band stations for the 2001 Anza, 2002 Yorba Linda, and 2003 Big Bear City earthquakes were provided by David Boore (USGS, written communication 2005). Peak acceleration values for many other events were supplied by Jack Boatwright (USGS, written communication 2005, 2006) or obtained from the TriNet website. Estimates of site conditions were provided by Chris Wills based on surface geology (Wills and Clahan 2006) and by Jack Boatwright. The TriNet data were used to provide additional guidance on functional forms and provide additional constraints on coefficients of the ground motion model (Chiou and Youngs 2008).

MODEL FORMULATION

Using algebraic expressions to represent the average behavior observed in the empirical strong-motion data, the empirical ground motion model developed here attempts to capture the effects of the amount of energy radiated at the source, the attenuation of seismic waves along the path due to geometric spreading and energy absorption, and local modification of the seismic waves by the near-surface materials. The form of these expressions is guided by trends in the data, simple seismological models, past experience, and examination of the results of ground motion simulations conducted as part of the PEER-NGA project.

SEISMIC SOURCE SCALING

Effect of Earthquake Size

We use moment magnitude as the simplest measure for correlating the amount of energy released in an earthquake with the resulting amplitudes of ground motions. Many empirical ground motion models, including Sadigh et al. (1997), use a polynomial function for scaling the \ln of ground motions y with magnitude of the form:

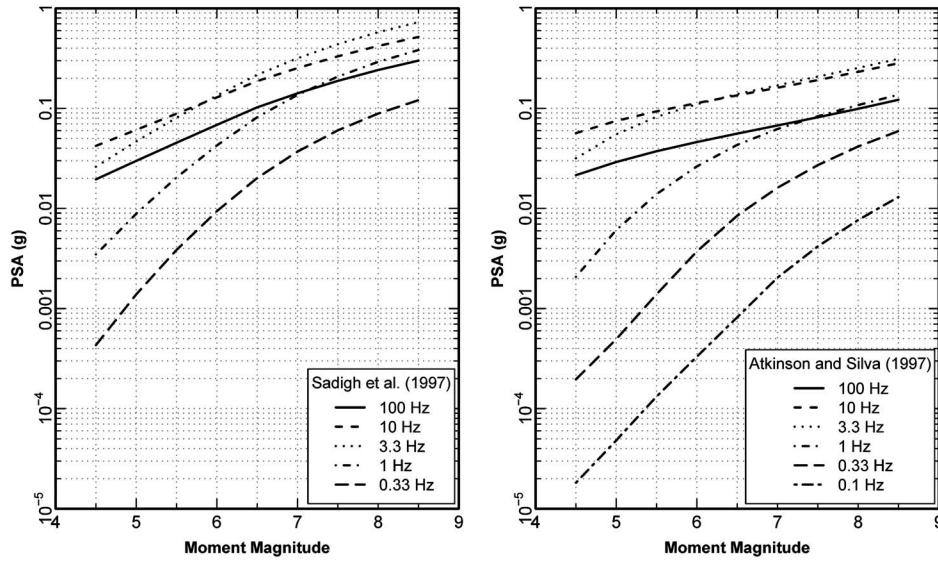


Figure 2. Magnitude scaling of pseudo spectral acceleration at a distance of 30 km computed using (left) Sadigh et al. (1997) and (right) the stochastic ground motion model and the Atkinson and Silva (1997) source model for California earthquakes.

$$\ln(y) \propto C_2(T) \times \mathbf{M} + C_3(T) \times (m_C - \mathbf{M})^n \quad (2)$$

where coefficients C_3 and possibly C_2 vary with spectral period T , the exponent n is typically in the range of 2 to 3, and coefficient m_C is independent of T . The left hand plot of Figure 2 shows the magnitude scaling of pseudo spectral acceleration, y , at a rupture distance of 30 km obtained from the Sadigh et al. (1997) ground motion model.

In contrast, seismological models for earthquake source spectra suggest an alternative form for magnitude scaling. The right hand plot of Figure 2 shows magnitude scaling relationships at a distance of 30 km computed using the stochastic ground motion model (e.g., Boore 2003) and the Atkinson and Silva (1997) empirical source spectra model for California earthquakes. For spectral frequencies of 10 Hz and higher the magnitude scaling of $\ln(y)$ is approximately linear at a relatively flat slope in the magnitude range of $5 \leq \mathbf{M} \leq 8.5$, representing scaling of the source spectrum above the corner frequency. For frequencies of 0.3 Hz and lower the magnitude scaling in the range of $5 \leq \mathbf{M} \leq 7$ is again approximately linear, but at a much larger slope than for high-frequency motions, reflecting scaling of the source spectrum below the corner frequency. The transition between the two approximately linear scaling regions occurs over the magnitude range where the corner frequency of the source spectrum is near the spectral frequency of the ground motion. As the spectral frequency of the ground motions decreases, the magnitude range for this transition shifts to larger magnitudes, reflecting the decrease in corner frequency with increasing magnitude.

The shape of the magnitude scaling curves shown in the right hand plot of Figure 2 is modeled by the expression:

$$\ln(y) \propto c_2 \mathbf{M} + \frac{1}{c_n} (c_2 - c_3) \times \ln[1 - \exp\{c_n(c_{\mathbf{M}} - \mathbf{M})\}] \quad (3)$$

In Equation 3 coefficient c_2 is the slope of the magnitude scaling relationship for earthquakes whose theoretical corner frequency is well above the spectral frequency of interest and c_3 is the slope for earthquakes whose corner frequency is well below the spectral frequency. Coefficient c_n controls the width of the magnitude range over which the transition from c_2 scaling to c_3 scaling occurs. Coefficient $c_{\mathbf{M}}$ is the magnitude at the midpoint of this transition and its value varies with the spectral period of the ground motion parameter y . In Equation 3, c_3 represents scaling of ground motion spectra below the corner frequency where the source spectra are directly proportional to seismic moment, M_0 . Because $\mathbf{M} \propto 2/3 M_0$, theoretically, c_3 should equal $1.5 \times \ln(10)$ or 3.45 and so it is fixed at this value. Simulations based on the updated source spectral model for California earthquakes defined by Atkinson and Silva (2000) produces scaling of $\ln(y) \propto 1.06 \mathbf{M}$. In the Sadigh et al. (1997) form of Equation 2, coefficient C_2 also represents the magnitude scaling of the source spectra at distances large enough that the source can be considered a point. The Sadigh et al. (1997) values of C_2 were 1.0 to 1.1. Therefore, coefficient c_2 was fixed at 1.06. Coefficients c_n and $c_{\mathbf{M}}$ were obtained by fitting the strong motion data.

The empirical data are not sufficient to distinguish between magnitude-scaling defined by Equations 2 and 3. We prefer the scaling form of Equation 3 because we believe that it better represents our current concept of earthquake source spectra scaling with earthquake magnitude.

Style of Faulting Effects

Our exploratory analysis of the NGA data indicated that reverse faulting earthquakes produce larger high-frequency motions than strike-slip earthquakes. This effect diminishes as the spectral period increases, with the motion from strike-slip earthquakes becoming the larger of the two at long periods, similar to findings by other investigators (e.g., Abrahamson and Silva 1997; Campbell and Bozorgnia 2003; Ambraseys et al. 2005). Chiou et al. (2000) showed that when the geometric hanging-wall effect was accounted for by using the R_{RMS} distance measure, reverse-faulting earthquake still produced statistically significant higher motions than strike-slip earthquakes.

Some empirical models have shown that normal-faulting/extensional regime earthquakes produce lower ground motions than strike-slip earthquakes (e.g., Spudich et al. 1999; Ambraseys et al. 2005) while others have included normal-faulting and strike-slip together in a single class (e.g., Abrahamson and Silva 1997; Sadigh et al. 1997; Campbell and Bozorgnia 2003). In our exploratory analysis of NGA data the style of faulting effect for normal faults was found to be statistically significant (p-values slightly less than 0.05) only when normal faulting was restricted to rake angles, λ , in the range of -120° to -60° ; with normal-oblique earthquakes included in the same style-of-faulting class as strike-slip earthquakes.

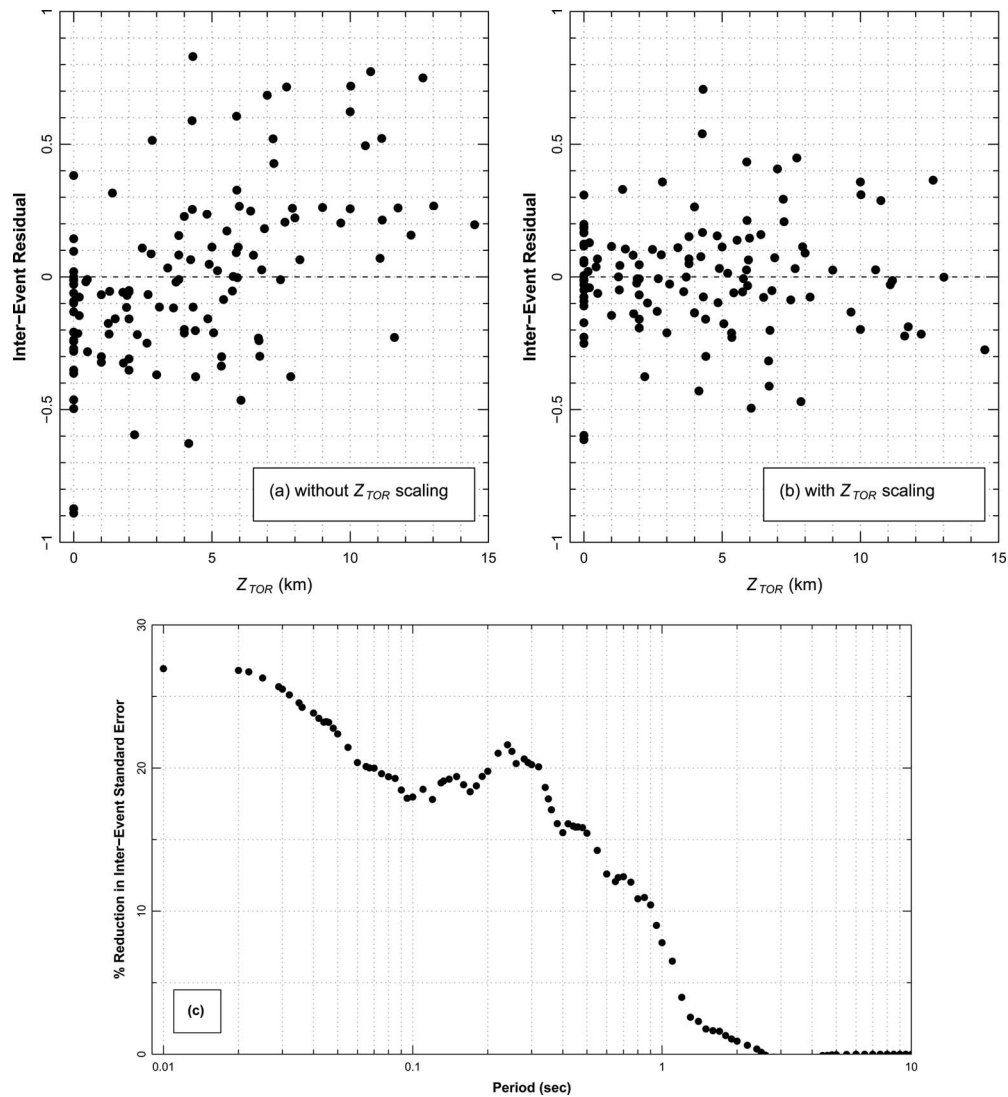


Figure 3. Effect of source depth on inter-event residuals. (a) *PGA* data fit without Z_{TOR} scaling. (b) *PGA* data fit with Z_{TOR} scaling. (c) Reduction in inter-event standard error resulting from including Z_{TOR} scaling.

Other Source Effects

Other source parameters examined include source depth and main shock-aftershock differences. In the preliminary analyses it was found that the NGA data exhibited a statistically significant dependence on source depth parameterized as the depth to top of rupture, Z_{TOR} , and that aftershocks showed a stronger dependence on Z_{TOR} than main shocks. Figure 3 shows inter-event residuals for models fit to the *pga* data without and

with Z_{TOR} scaling. The inter-event residuals for the fit without Z_{TOR} scaling show a clear trend while those for the fit with Z_{TOR} scaling do not. Part c of Figure 3 shows the percent reduction in inter-event standard error obtained by including Z_{TOR} scaling.

As indicated above, we include aftershocks in our analyses to provide additional data to help constrain the coefficients of the site response model. We found that aftershocks tend to produce lower motions than main shocks with similar magnitudes. Hence we included this difference in the ground motion model. We also found that the style of faulting effects were much weaker for aftershocks than for main shocks. Therefore, the ground motion model incorporates separate depth-dependence for main shocks and aftershocks and no style of faulting effects for aftershocks.

PATH SCALING

The scaling or attenuation of ground motion amplitude with distance from the earthquake rupture involves two primary effects, geometric spreading and energy absorption along the travel path due to material damping and wave scattering. In most empirical ground motion models these effects are modeled by the functional form:

$$\ln(y) \propto C_{Geometric} \times \ln[(R^n + C_{Source_Size}^n)^{1/n}] + \gamma \times R \quad (4)$$

where $C_{Geometric}$ defines the rate of attenuation due to geometric spreading, γ defines the rate of anelastic attenuation, typically quantified in terms of the quality factor Q . Coefficient C_{Source_Size} accounts for the effect of the source size on geometric spreading. Coefficient $C_{Geometric}$ interacts with C_{Source_Size} and n to define distance scaling at small distances from the source and interacts with γ to define distance scaling at large distances from the source. These two interactions are examined below.

Near-Source Distance Scaling

Of foremost interest to engineering application in active tectonic regions is the effect of extended source dimensions that leads to magnitude-dependent attenuation rates within the distance range of 0 to 50 km or more. The consequence of this effect is what has been termed near-source saturation—less magnitude scaling at small source-site distances than at large source-site distances. Two approaches have been used to model this effect within the framework defined by Equation 4. One approach uses a magnitude-independent value of $C_{Geometric}$ combined with a magnitude-dependent value for C_{Source_Size} [e.g., Sadigh et al. (1997) with exponent $n=1$; Campbell (1993) and Campbell and Bozorgnia (2003) with $n=2$]. The alternative approach has been to use a magnitude-dependent value for $C_{Geometric}$ combined with a magnitude-independent value for C_{Source_Size} [e.g., Idriss (1991, written communication 2002) with $n=1$; Abrahamson and Silva (1997) with $n=2$]. Figure 4 illustrates the behavior of these approaches to distance scaling as implemented in recent ground motion models. The effect of the value of the exponent n is seen by comparing the models shown on the left for exponent $n=1$ to those shown on the right with $n=2$. Use of $n=2$ results in the rate of attenuation approaching the value defined by $C_{Geometric}$ at relatively short distances, allowing an interpretation of its value as a direct estimate of the rate of geometric spreading. Use of $n=1$ results in the attenuation rate approaching the value of $C_{Geometric}$ slowly and its

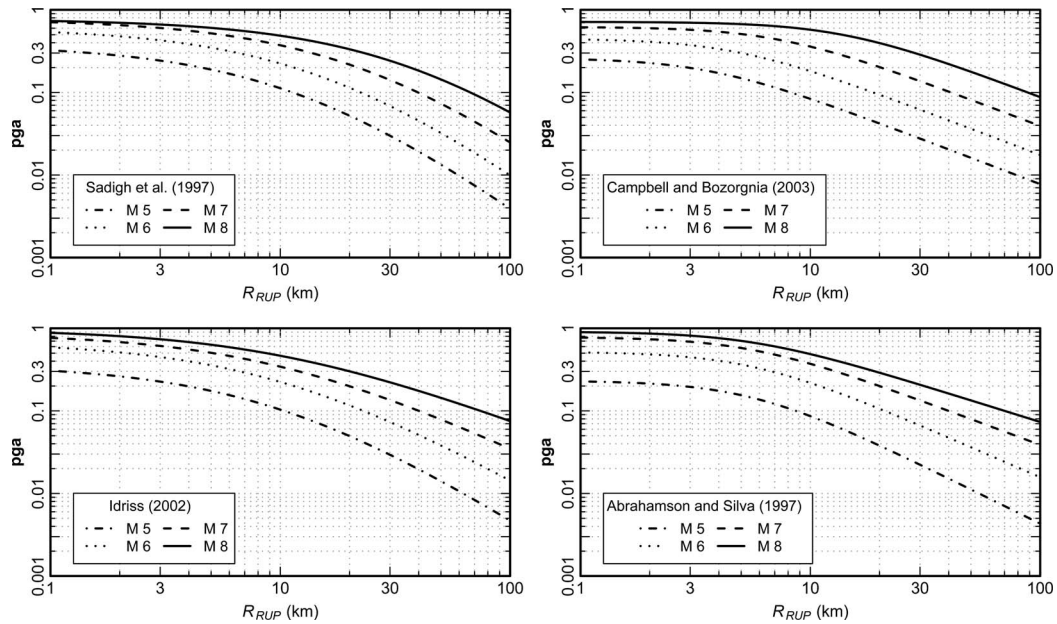


Figure 4. Illustration of functional forms used to capture magnitude-dependence of distance attenuation. All plots are for rupture distance to a vertical strike-slip fault rupturing the surface. The values for Campbell and Bozorgnia (2003) were computed using R_{SEIS} equal to 3 km.

value cannot be directly equated with the rate of geometric spreading at distances less than 50 km. The different implementations of Equation 4 shown in Figure 4 also produce differences in ground motion scaling with magnitude at large distances from the source. The models that use a magnitude-independent $C_{Geometric}$ (top row of Figure 4) approach distance-independent magnitude scaling at large distances while those that use magnitude-dependent $C_{Geometric}$ produce distant-dependent magnitude scaling at all distances.

Based on our examination of the alternative forms of Equation 4 we conclude that they all provide reasonable fits to the empirical data. Discrimination among them would require a great deal more data at distances less than 10 km. The data show magnitude-dependence in the rate of attenuation at all distances. However, we believe that the mechanisms that cause this behavior may be different at different distances. At distances less than ~ 50 km, magnitude-dependence is due to the effect of extended sources. This effect can be modeled by all of the functional forms shown in Figure 4. However, at large distances, >100 km, we think that another effect may be causing magnitude-dependence in the attenuation of response spectral ordinates—the interaction of path Q with the differences in source Fourier spectra as a function of magnitude. This concept is explored below. We prefer to use a model form that allows for separation of the effect of

magnitude at small and at large distances, and therefore select the magnitude-independent form of $C_{Geometric}$. This form allows the use of Equation 3 to define magnitude scaling at large distances from the source.

We examined the alternatives for the exponent n . As shown by the upper right-hand plot in Figure 4, use of $n=2$ allows the model to approach a constant geometric spreading rate at distances greater than about $2 \times C_{Source_Size}$. After experimenting extensively with this form, we concluded that $n=2$ resulted in too little distance scaling over the distance range of 0 to 10 km for large-magnitude earthquakes, and we use exponent $n=1$, resulting in the form used by Sadigh et al. (1997). Instead of the piece-wise linear model for C_{Source_Size} used by Sadigh et al. (1997), we use a smooth transition in the magnitude scaling over the full magnitude range accomplished by using the relationship:

$$C_{Source_Size}(\mathbf{M}) = c_5 \cosh\{c_6 \max(\mathbf{M} - 3, 0)\} \quad (5)$$

The use of Equation 5 has the property that C_{Source_Size} varies smoothly from a constant at small magnitudes to $C_{Source_Size} \propto \exp(c_6 \mathbf{M})$ at large magnitudes.

Path Scaling at Large Distances

Many studies of the attenuation of ground motion Fourier amplitudes with distance indicate that there is a change in the rate of geometric spreading from approximately proportional to $1/R$ at short distances to $1/\sqrt{R}$ at large distances, with this transition occurring in the range of 40 to 70 km. This change has been interpreted to be the combination of the effects of post-critical reflections from the lower crust and transition from direct body wave to Lg wave spreading (e.g., Atkinson and Mereu 1992). Models of the decay of Fourier spectra with distance in California have found or assumed that the geometric spreading is proportional to $1/\sqrt{R}$ for distances greater than 40 km (Raouf et al. 1999; Erickson et al. 2004) and this form of geometric spreading was used by Atkinson and Silva (2000) to model strong ground motions. Earlier, Atkinson and Silva (1997) used a tri-linear form of attenuation similar to that defined by Atkinson and Mereu (1992), but indicated that a bi-linear form would also work as well.

We explored this effect by modeling spectral accelerations from 666 broadband recordings from three small Southern California earthquakes (2001 Anza, \mathbf{M} 4.92; 2002 Yorba Linda, \mathbf{M} 4.27; and 2003 Big Bear City, \mathbf{M} 4.92; NGA events 0163, 0167, and 0170, respectively). These data were fit with three functional forms: a model with a single value of $C_{Geometric}$ at all distances (1-slope model), a model in which $C_{Geometric}$ at large distances becomes one-half of the value at small distances (2-slope model), and a model in which $C_{Geometric}$ is fixed at -0.5 for larger distances (2-slope, 2nd fixed model). Site effects were modeled as a linear function of $\ln(V_{S30})$ as little nonlinear behavior is expected at the level of motions recorded in these earthquakes. The analysis was conducted for spectral periods in the range of 0.01 to 5 seconds (frequencies from 100 to 0.2 Hz) (see Chiou and Youngs 2008 for details). At all spectral periods, the 2-slope models produced slightly smaller standard errors than the 1-slope model. The location for the break in slope varied between 40 and 60 km. In addition, use of the

1-slope model produces unrealistic positive values of the anelastic attenuation coefficient γ for longer period motions, a fact also noted by Atkinson and Silva (1997).

Examination of TriNet *pga* data from many of the better-recorded small magnitude earthquakes shows that there is a decrease in the rate of attenuation at distances in the range of 40 to 70 km (Chiou and Youngs 2008). Tests of the PEER-NGA data also show that a two-slope model is statistically significant with a slope break also in the range of 45 to 60 km. Examination of the 1-D rock numerical simulation data (Somerville et al. 2006) also indicate that a two-slope model provides a good fit with a break in slope at about 60 km.

Based on the above observations, we adopted the concept of a change in the rate of attenuation occurring at some transition distance. If one were to use an abrupt transition point, then the best fit transition point may vary from earthquake to earthquake as a function of a number of parameters including source depth, source size, and the local crustal thickness. Instead, we use a smooth transition over a broad distance range to provide an average fit to the behavior observed in the data.

Equation 6 defines the formulation used for distance attenuation. It incorporates magnitude-dependent extended source effects, potentially magnitude-dependent wave propagation effects on response spectra at large distances, and a smooth transition from dominance of ground motions by direct waves at small distances, modeled by attenuation coefficient c_4 , to dominance by *Lg* waves at large distances, modeled by attenuation coefficient c_{4a} .

$$\ln(y) \propto c_4 \ln[R_{RUP} + c_5 \cosh\{c_6 \max(\mathbf{M} - 3, 0)\}] + (c_{4a} - c_4) \ln \sqrt{R_{RUP}^2 + c_{RB}^2} + \gamma(\mathbf{M}) R_{RUP} \quad (6)$$

Coefficient c_4 was examined by analyses of PEER-NGA data and TriNet data. It was concluded that a range of values for c_4 would provide satisfactory fits to the data with adjustments to the rate of near-source attenuation occurring through changes of coefficients c_5 and c_6 . Therefore, c_4 was fixed at -2.1 , the value obtained originally by Sadigh et al. (1997) for rock sites.

Coefficient c_{RB} defines the midpoint of the transition in distance scaling. As discussed above similar transition points were found from analyses of the extended data sets for the three small southern California earthquakes, the NGA data, and the 1-D rock simulations. We therefore, set the value of c_{RB} to be 50 km, the central value of the estimates we obtained from the various data sets.

The appropriate value of the attenuation rate at distances beyond c_{RB} , coefficient c_{4a} , cannot be readily determined from the data because it is highly correlated with the assessment of the anelastic attenuation coefficient γ , as had been noted by many previous investigators (e.g., Atkinson 1989; Frankel et al. 1990). Therefore, we assume that the rate of attenuation at distances beyond 50 km is modeled by c_{4a} equal to -0.5 and let the anelastic attenuation coefficient γ account for departures from this value.

The anelastic attenuation coefficient γ is allowed to be magnitude dependent. Boatwright et al. (2003) found magnitude-dependence in the anelastic attenuation coefficient from their study of pga and pgv from northern California ShakeMap data, with increasing magnitude producing smaller absolute values of γ (less energy absorption). In addition, stochastic simulations of ground motions using a magnitude-independent Q model produce magnitude-dependence in the resulting anelastic attenuation coefficient γ obtained from fits to response spectra ordinates (e.g., Campbell 2003). This effect was also noted in our fitting of ground motions simulated using the Atkinson and Silva (2000) ground motion model. The effect is likely due to a shift to lower frequency ground motion driving the response of a damped oscillator (and driving pga , Boatwright et al. 2003) as the size of the earthquake increases.

Data Truncation and $\gamma(M)$

The initial analyses of the PEER-NGA data suggested that the anelastic attenuation coefficient γ in Equation 6 was 50-percent larger in absolute value for earthquakes in Taiwan than for earthquakes in California or the other active tectonic regions represented in the selected database. This would imply that Q for Taiwan was significantly lower than Q for California or the other regions. However, review of the literature failed to produce studies that confirmed this result. In addition, the estimates of γ obtained from the extensive broadband data for the three southern California earthquakes were inconsistent with the values obtained for California earthquakes from fitting the PEER-NGA data.

These results led us to consideration of the effects of missing response data on the estimation of ground motion model coefficients. Evidence of truncation of the PEER-NGA data is shown in Figure 5. The solid data points are pga values for the processed acceleration time histories in the PEER-NGA database. The open data points are additional pga values obtained from other recordings. The PEER-NGA data and the extended data for each earthquake were fit using a truncated regression model (Toro 1981; Bragato 2004) and the truncation levels shown by the dotted and dash-dotted lines, respectively, in Figure 5. For the Northridge earthquake, similar estimates of γ were obtained from the PEER-NGA and extended data set. However, for the other three earthquakes, the estimate of γ obtained from the PEER-NGA data set were approximately 2/3 of the values obtained from the extended data sets, indicating that truncated regression using the PEER-NGA data set tends to underestimate the appropriate absolute value of γ .

Extended pga and pgv data sets were developed for 18 earthquakes in the PEER-NGA database plus three additional recent California earthquakes (see Chiou and Youngs 2008 for details). Truncated regression analyses were performed for each earthquake with the resulting values shown in Figure 6. These analyses were performed using Equation 6 to model distance attenuation with coefficient c_{4a} fixed at -0.5 . The absolute values of γ computed using only PEER-NGA data were typically smaller than those obtained from the extended data. Based on these analyses we conclude that regression analyses using the PEER-NGA data will tend to underestimate the rate of anelastic attenuation at large distances due to data truncation and that the problem cannot be solved

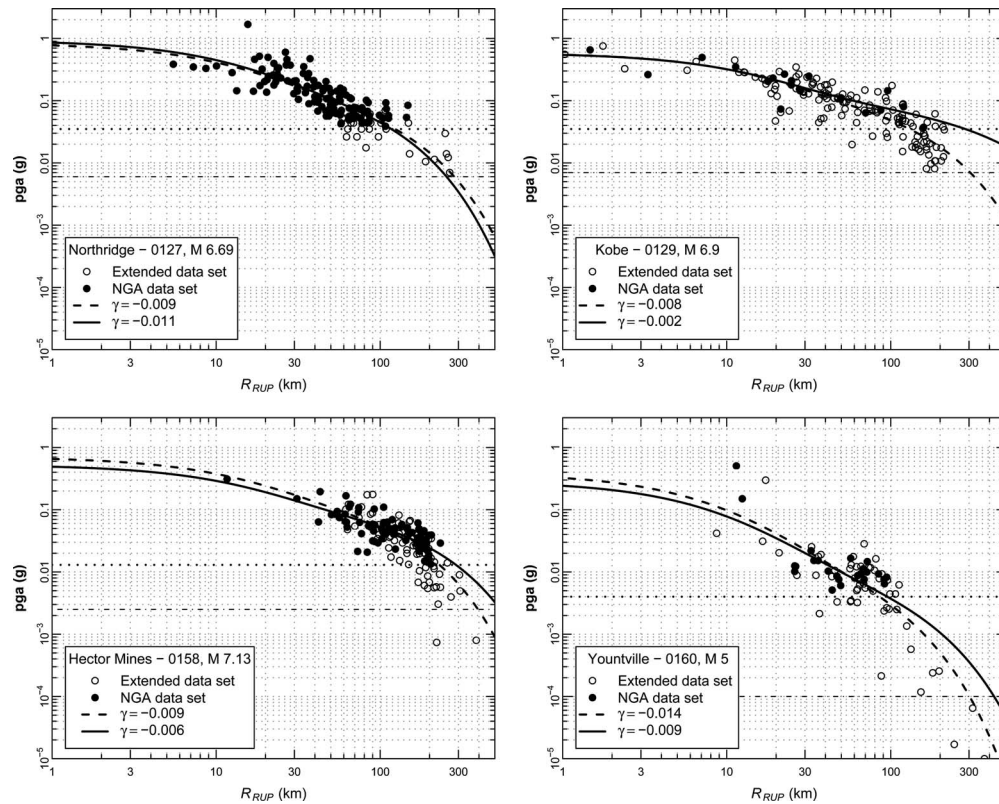


Figure 5. Comparison of fits to expanded data sets (open plus solid points, dashed curve) and PEER-NGA data only (solid points, solid curve) for individual earthquakes using truncated regression. Truncation levels are indicated by the horizontal dashed lines for the enhanced (dash-dot) and PEER-NGA only (dotted) data sets. Hanging-wall sites were not included in fits for Northridge.

using truncated regression. Our solution is to estimate the anelastic attenuation coefficient $\gamma(\mathbf{M})$ from the extended data sets developed for individual earthquakes. We then estimate the remaining coefficients of the model from the PEER-NGA data truncated at a maximum distance of 70 km. This distance was selected by visual inspection as the point where, on average, data truncation may begin to affect the distribution of recordings in the PEER-NGA database.

The values of γ obtained from the extended data sets show that γ decreases in absolute value with increasing magnitude, similar to results reported by others from analysis of empirical data (e.g., Campbell 1993) and stochastic ground motion simulations (e.g., Campbell 2003). Because we are interested primarily in modeling earthquake ground motions in the western United States, we develop a model for γ from the results for the 13 California earthquakes for which we developed extended data sets. The resulting relationship is:

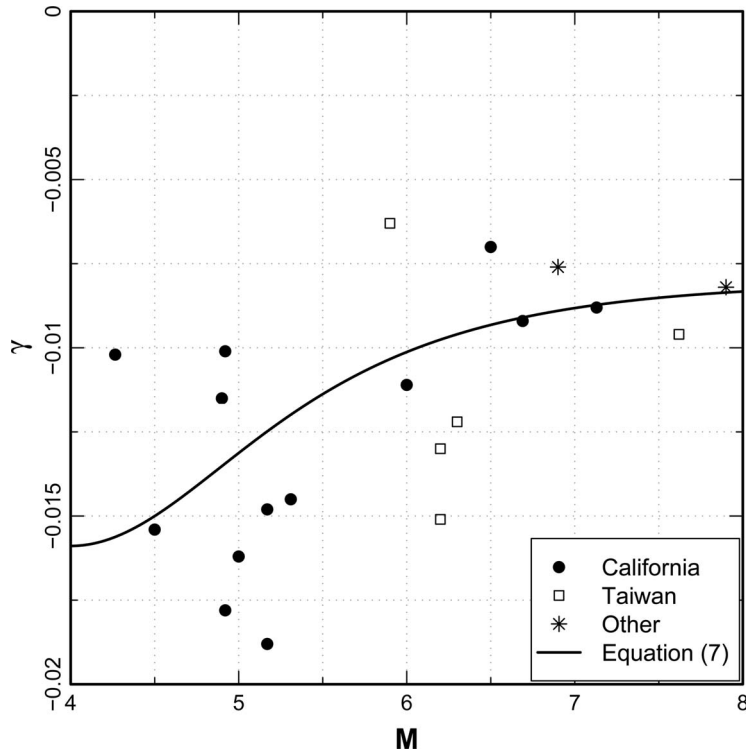


Figure 6. Estimates of γ for individual earthquakes and model fit to California earthquake data.

$$\gamma(pga)_{California} = -0.00804 - 0.00785/\cosh\{\max(\mathbf{M} - 4, 0)\} \quad (7)$$

This relationship is plotted on Figure 6. The limited data for earthquakes from other regions (Kobe, Japan; Denali, Alaska; Chi-Chi main shock and aftershocks, Taiwan) are generally consistent with this relationship. The data indicate that the value of γ for Taiwan may be slightly greater than that for California, but the difference is much less than the 50-percent larger values for Taiwan obtained from the initial regressions using the full PEER-NGA database. Equation 7 provides a relationship for γ at pga . The relationships for other spectral periods were constructed by scaling the period-dependent γ estimated from the broadband data for the three small southern California earthquakes by the relative difference in γ at pga .

Source-Site Geometry Effects

Based on analyses of ground motions from reverse earthquakes, Somerville and Abrahamson (1995) and Abrahamson and Somerville (1996) proposed the so called “hanging-wall” effect in which ground motions are enhanced in the hanging wall of reverse earthquakes. The effect was attributed to the inability of the R_{RUP} distance measure to capture the general proximity of a hanging wall site to rupture on the fault plane dip-

ping beneath it. Chiou et al. (2000) performed extensive analyses of empirical and numerical modeling data for reverse fault ruptures and reached the same conclusion. They were able to remove the hanging-wall effect by using a root-mean-squared distance measure, R_{RMS} . The hanging-wall effect is also seen in the 1-D rock ground motion simulations conducted for the PEER-NGA project (Somerville et al. 2006).

Abrahamson and Silva (1997) included the hanging-wall effect in their empirical ground motion model as a distance-dependent term with an abrupt switch from no effect to full effect as one crosses into the hanging-wall region. Boore et al. (1997) conclude that their use of R_{JB} implicitly accounts for the hanging-wall effect in that all sites directly above the rupture have $R_{JB}=0$. Campbell and Bozorgnia (2003) introduces a smooth variation in the hanging-wall effect by tapering the effect from a maximum at $R_{JB}=0$ to zero for $R_{JB}>5$ km.

We use the following model to represent the hanging-wall effect:

$$f_{HW} = F_{HW} \tanh\left(\frac{R_X \cos^2 \delta}{c_{9a}}\right) \times \left[1 - \frac{\sqrt{R_{JB}^2 + Z_{TOR}^2}}{R_{RUP} + 0.001}\right] \quad (8)$$

where δ is fault dip and R_X represents the site coordinate (in km) measured perpendicular to the fault strike from the surface projection of the updip edge of the fault rupture, with the downdip direction being positive. Parameter F_{HW} is 1 for $R_X \geq 0$ and 0 for $R_X < 0$. The behavior of f_{HW} is illustrated in Figure 7 for three magnitudes and two values of Z_{TOR} . The plots show the value of f_{HW} for sites located directly above or down dip of the rupture surface.

The motivation for Equation 8 is as follows. The second term serves several functions. Examination of the simulation results presented in Chiou et al. (2000) and those conducted for the NGA project (Somerville et al. 2006) indicated that the hanging-wall effect decreases to near zero as one approaches the updip edge of the rupture (R_X approaches 0). These data also show that this decrease extends to larger values of R_X as the fault dip increases, in essence the hanging-wall effect is projected further from the fault top. This effect, combined with the fact that the fault width decreases as the magnitude decreases, produces a decrease in the hanging-wall effect with decreasing magnitude. The third term of Equation 8 is motivated by the modeling of Boore et al. (1997) and Campbell and Bozorgnia (2003) in that f_{HW} decreases as R_{JB} increases. Placing R_{RUP} in the denominator of this term produces a smooth transition in the spatial extent of the hanging-wall effect at various locations in the hanging wall. For sites not directly above but near the top of the rupture, R_{RUP} is only slightly larger than R_{JB} and f_{HW} decreases rapidly as one moves away from the rupture. For sites near the bottom edge of the rupture $R_{RUP} \gg R_{JB}$ and f_{HW} decreases more slowly as one moves away from the rupture. The value of 0.001 km is added to provide numerical stability when R_{RUP} equals 0. The term $\sqrt{R_{JB}^2 + Z_{TOR}^2}$ is used to model the decrease in the hanging-wall effect with increasing depth of rupture observed in the PEER-NGA data and in the study by Chiou et al. (2000).

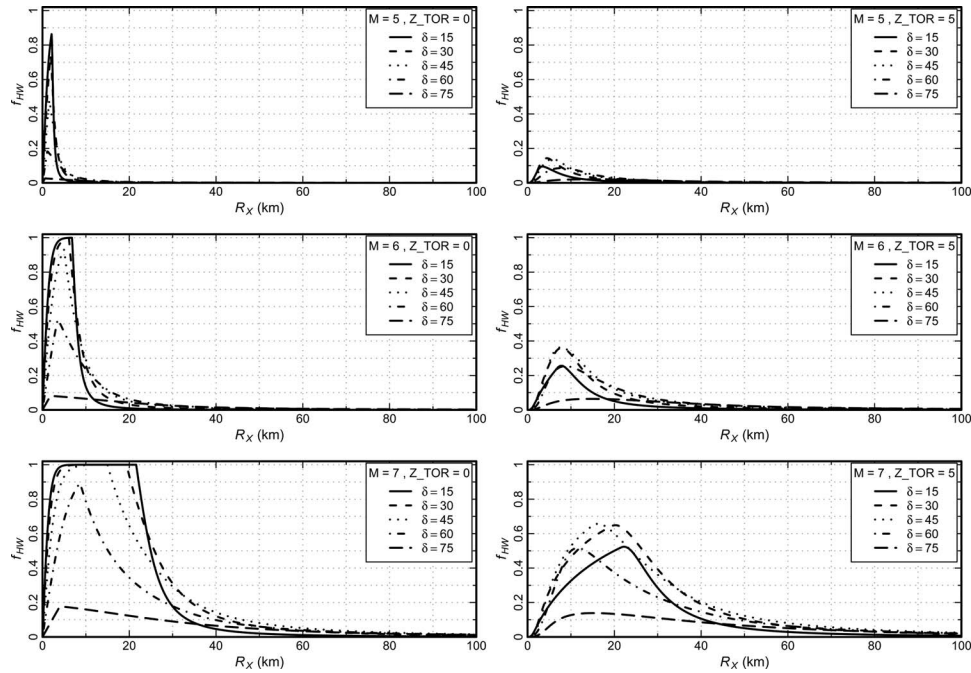


Figure 7. Illustration of the hanging wall geometric factor f_{HW} for sites located directly above or down dip of the rupture plane. Plots on left are for M 5, 6, and 7 earthquakes with $Z_{TOR}=0$. Plots on right are for M 5, 6, and 7 earthquakes with $Z_{TOR}=5$ km. Note that the locations of the bottom edge of the ruptures correspond with the peaks in the f_{HW} curves.

SITE EFFECTS

Near-Surface Geology

The incorporation of the effects of near-surface geology or site classification has gone through an evolution in the past 10 years. At the beginning of this period, ground motion models typically contained a scaling parameter based on site classification (e.g., Boore et al. 1993), or presented different models for “rock” and “soil” sites (e.g., Campbell 1993; Sadigh et al. 1997). Classification of recording sites into rock or soil sites varied among investigators. Boore et al. (1997) introduced the explicit use of the average shear-wave velocity in the upper 30 meters, V_{S30} , in the ground motion model. Abrahamson and Silva (1997) building on an earlier model by Youngs (1993) introduced the explicit modeling of non-linear site effects in the ground motion model. The model we have developed for incorporating near-surface geology combines these concepts using the formulation:

$$\ln(y) = \ln(y_{ref}) + f_{site}(V_{S30}, y_{ref}) \quad (9)$$

The parameter y_{ref} is the ground motion on the reference site condition derived from the source and path scaling models described in the previous sections. The reference site

V_{S30} was chosen to be 1130 m/sec because it is expected that there will not be significant nonlinear site response at this velocity. In addition, there are very few data with values of V_{S30} greater than 1100 m/sec in the PEER-NGA database. The reference motion is defined to be the spectral acceleration at the spectral period of interest for two reasons. Bazzurro and Cornell (2004) indicate that the spectral acceleration at spectral period T is “the single most helpful parameter” for the prediction of site amplification at that period. In addition, the estimation of the coefficients of the ground motion model is performed using random (mixed) effects regression in which the reference motion includes the random event term representing the deviation of the average ground motions for a given earthquake from the global population mean. Use of the reference spectral acceleration at period T to estimate surface ground motions at the same period eliminates the need to include the correlation in the random effects between those at period T and those at another period or pga .

The function form for the site response model f_{site} with y_{ref} computed at V_{S30} equal to 1130 m/sec is given by:

$$f_{site}(V_{S30}, T, y_{ref}) = a(V_{S30}, T) + b(V_{S30}, T) \ln \left[\frac{y_{ref}(T) + c(T)}{c(T)} \right]$$

$$a(V_{S30}, T) = \phi_1(T) \ln \left[\frac{V_{S30}}{1130} \right]$$

$$b(V_{S30}, T) = \phi_2(T) [\exp\{\phi_3(T) \times (\min(V_{S30}, 1130) - 360)\} - \exp\{\phi_3(T) \times (1130 - 360)\}]$$

$$c(T) = \phi_4(T) \quad (10)$$

The interpretation of the coefficients a , b , and c is as follows. Coefficient a represents the linear site response that occurs at small level of reference site motion. It is modeled as a linear function of $\ln(V_{S30})$ consistent with previous representations (e.g., Boore et al., 1997). Coefficient c represents the reference ground motion level in the middle of the transition from linear to nonlinear behavior. Coefficient b represents the degree of nonlinear behavior in terms of a decrease in site amplification, f_{site} , with increasing amplitude of the reference motion. In general, a stronger nonlinearity in soil response corresponds to a more negative value for b (stronger dependence on y_{ref}). It is expected that the degree of nonlinearity is a function of the stiffness of the site soils and this effect is represented by making b a function of V_{S30} . The last term of the equation for b is used to produce linear response ($b=0$) for $V_{S30}=1,130$ m/sec. Figure 8 shows examples of f_{site} obtained from fitting the PEER-NGA data. The functional form of Equation 10 is able to represent other models of nonlinear site response, such as that developed by Choi and Stewart (2005) as well as the results of site response analyses conducted for the NGA project by Walling et al. (2008).

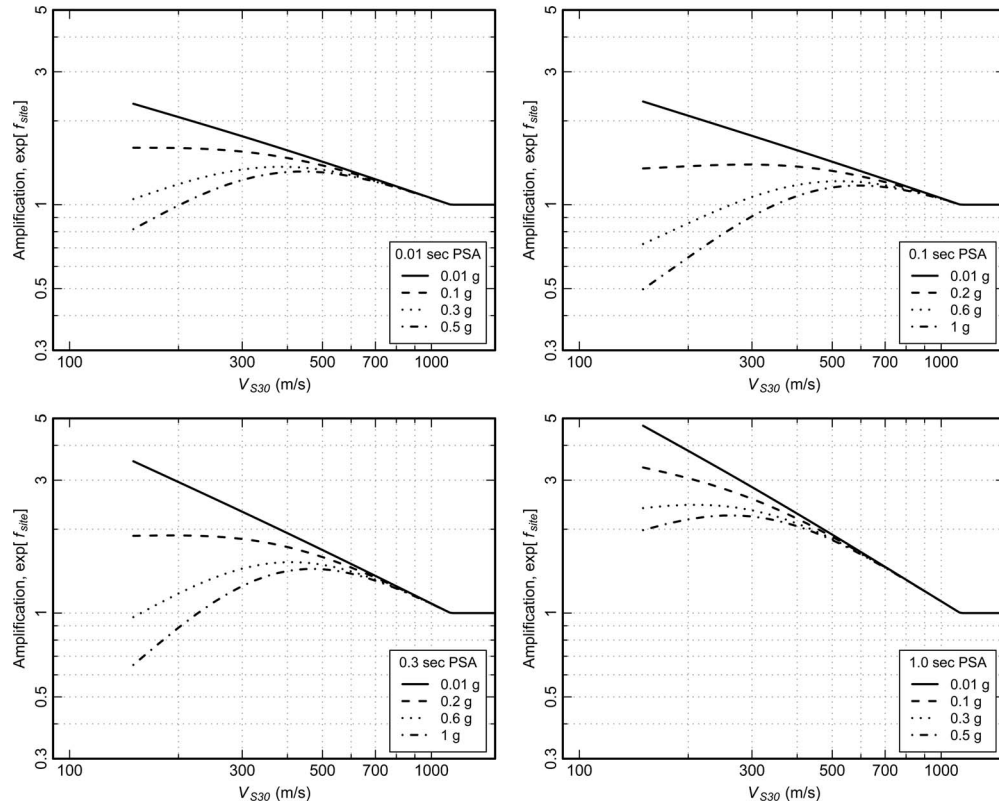


Figure 8. Example site amplification as a function of spectral period, V_{S30} , and level of reference *PSA*.

Sediment Thickness

Most empirical ground motion models have used either a simple classification scheme (e.g., Abrahamson and Silva 1997; Sadigh et al. 1997) or V_{S30} (e.g., Boore et al. 1997) to represent soil amplification in ground motions. The success of these models suggests that surface geology or V_{S30} is often highly correlated with other site properties important to the quantification of site amplification. However, a single parameter such as V_{S30} cannot be expected to completely represent the effects of local site conditions on earthquake ground motions. Campbell (1989) found that adding a parameter for depth to basement rock improved the predictive ability of empirical ground motion models. Other investigator had proposed that including basin depth leads to improved empirical ground motion models (e.g., Joyner 2000; Field 2000; Choi et al. 2005). In addition, successful modeling of ground motions on a variety of site conditions with numerical methods incorporate a much more detailed characterization of the site velocity profile (e.g., Silva et al. 1996; Boore and Joyner 1997).

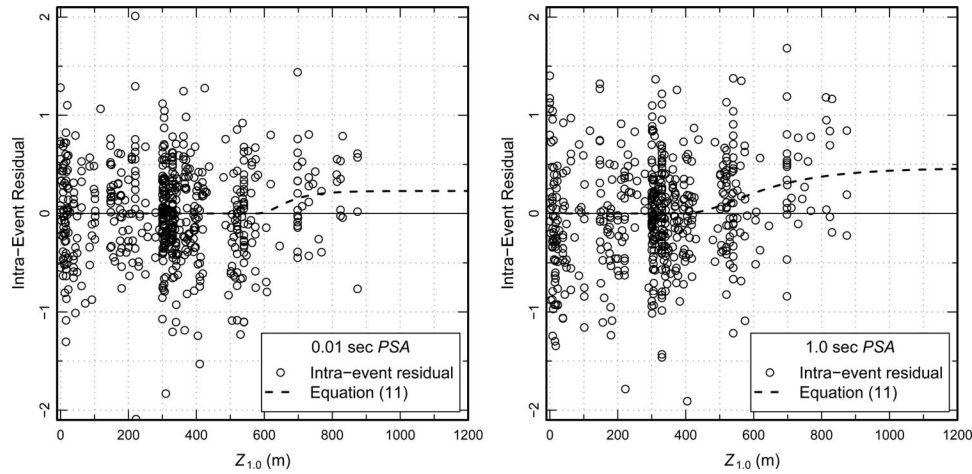


Figure 9. Intra-event residuals plotted against measured $Z_{1.0}$ for 0.01-sec and 1.0-sec *PSA*. The dashed lines show fits to the residuals using Equation 11.

To improve the modeling in such environments, we add sediment thickness as a second predictor of site amplification. We define sediment thickness as the depth to a material (bedrock) with a shear-wave velocity (V_S) of 1 km/sec or greater. Shear-wave velocities of 1.5 km/sec and 2.5 km/sec have also been used to define the appropriate velocity horizon (e.g., Field 2000; Day et al. 2006). We prefer 1 km/sec because it is similar to values commonly used in practice for rock. It is also close to the reference V_{S30} (1130 m/sec) used in the scaling of soil amplification. Finally, the depth to this velocity is more likely to be available as a part of site characterization than depths to higher velocity horizons. For example, boreholes at 54 sites in the PEER-NGA database penetrated the $V_S=1$ km/sec horizon.

Deep Sediment Sites

Figure 9 shows residuals from an interim model without a sediment depth effect plotted versus $Z_{1.0}$ for sites in the PEER-NGA database with values of $Z_{1.0}$ obtained from site velocity profiles or the regional velocity models described above. We find that the trend can be adequately modeled by the functional form:

$$\ln(y) \propto \phi_5 \left(1 - \frac{1}{\cosh[\phi_6 \times \max(0, Z_{1.0} - \phi_7)]} \right) \quad (11)$$

This functional form produces behavior similar to the model developed by Day et al. (2006, 2008), allowing for the fact that Day et al. (2006) modeled the combined effect of V_{S30} and sediment depth using only sediment depth while the residuals shown in Figure 9 are computed from a model that incorporates V_{S30} scaling. The main difference from Day et al. (2006, 2008) is that we allow the affected $Z_{1.0}$ range ($Z_{1.0} > \phi_7$) to vary with

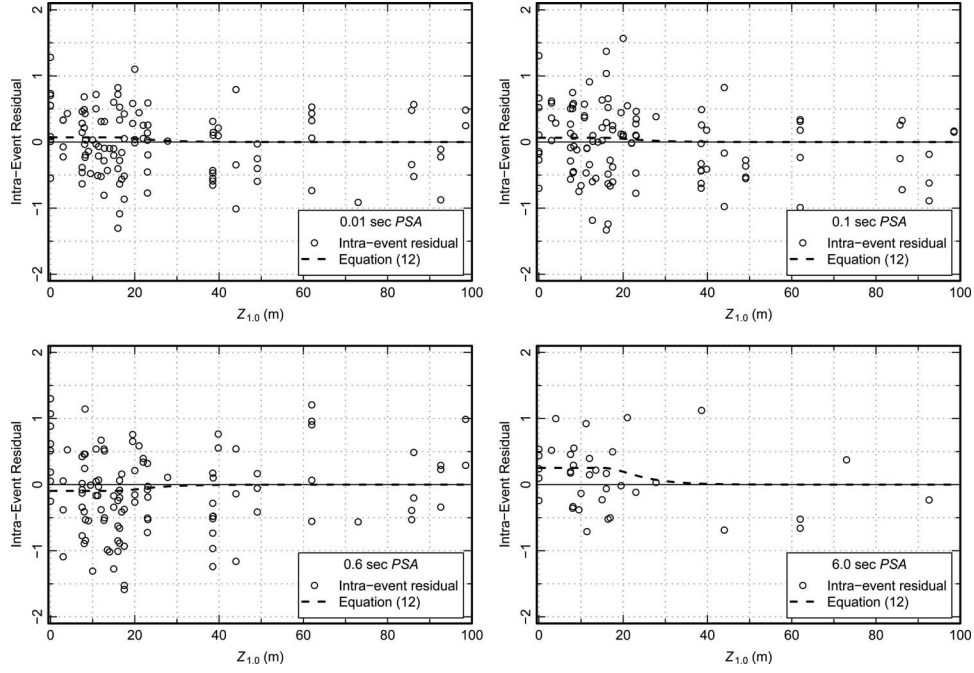


Figure 10. Intra-event residuals plotted against $Z_{1,0}$ for shallow sediment sites for spectral periods of 0.01, 0.10, 0.6, and 6.0 seconds. The dashed lines show fits to residuals using Equation 12.

spectral period, motivated by observing this trend in the residuals (Figure 9). The fitted models are shown on Figure 9.

Shallow Sediment Sites

Figure 10 shows residuals from an interim model without a sediment depth effect plotted versus $Z_{1,0}$ for those sites in the PEER-NGA data base with measured values of $Z_{1,0}$. We find negative average residuals in the $Z_{1,0}$ range of 5 to 25 m for spectral periods between 0.3 and 1 seconds and positive residuals at other periods. Because of the limited data available to determine the $Z_{1,0}$ at which average residual is back to 0, we judged a value of 40 m to be reasonable, and use the following functional form to model the $Z_{1,0}$ effect on shallow rock sites:

$$\ln(y) \propto \frac{\phi_8}{\cosh(0.15 \times \max(0, Z_{1,0} - 15))} \quad (12)$$

For the majority of sites there is a high correlation between V_{S30} and $Z_{1,0}$ and the effects of site geology on ground motion are generally captured by the V_{S30} scaling defined by Equation 10. The intent of Equations 11 and 12 is to capture departures from this general scaling.

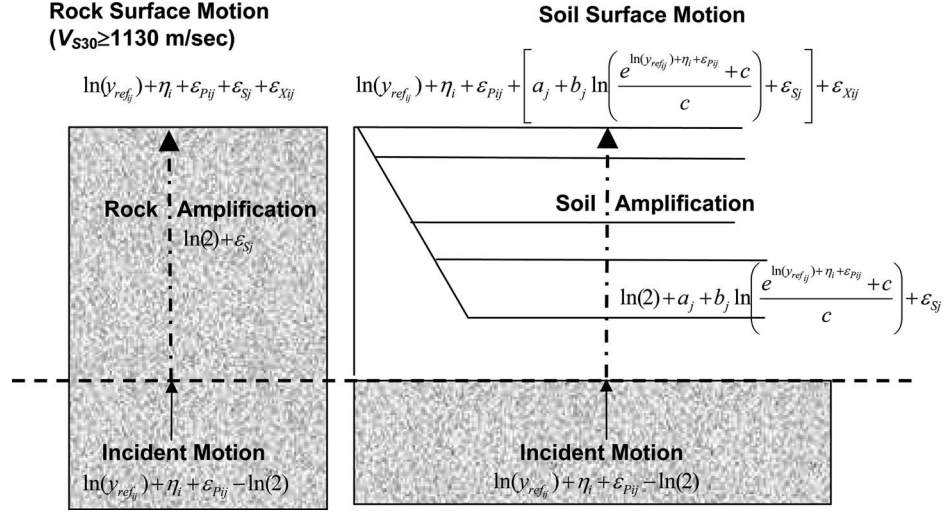


Figure 11. An illustration showing the framework of rock surface motion, soil amplification, and soil surface motion. It is assumed that ε_S has the same probability density function for rock and soil surface motions.

COMBINED MODEL FOR ESTIMATING GROUND MOTIONS

The complete model formulation is given by:

$$\begin{aligned}
 \ln(y_{ref_{ij}}) = & c_1 + [c_{1a}F_{Rvi} + c_{1b}F_{NMi} + c_7(Z_{TORi} - 4)](1 - AS_i) + [c_{10} + c_{7a}(Z_{TORi} - 4)]AS_i \\
 & + c_2(\mathbf{M}_i - 6) + \frac{c_2 - c_3}{c_n} \ln(1 + e^{c_n(c_M - \mathbf{M}_i)}) \\
 & + c_4 \ln[R_{RUPij} + c_5 \cosh\{c_6 \max(\mathbf{M}_i - c_{HM}, 0)\}] \\
 & + (c_{4a} - c_4) \ln(\sqrt{R_{RUPij}^2 + c_{RB}^2}) \\
 & + \left\{ c_{\gamma 1} + \frac{c_{\gamma 2}}{\cosh[\max(\mathbf{M}_i - c_{\gamma 3}, 0)]} \right\} R_{RUPij} \\
 & + c_9 F_{HWij} \tanh\left(\frac{R_{Xij} \cos^2 \delta_i}{c_{9a}}\right) \left\{ 1 - \frac{\sqrt{R_{JBij}^2 + Z_{TORi}^2}}{R_{RUPij} + 0.001} \right\}
 \end{aligned} \tag{13a}$$

and

$$\begin{aligned}
\ln(y_{ij}) = & \ln(y_{ref_{ij}}) + \phi_1 \cdot \min\left(\ln\left(\frac{V_{S30j}}{1130}\right), 0\right) \\
& + \phi_2 \{e^{\phi_3(\min(V_{S30j}, 1130) - 360)} - e^{\phi_3(1130 - 360)}\} \ln\left(\frac{y_{ref_{ij}} e^{\eta_i} + \phi_4}{\phi_4}\right) \\
& + \phi_5 \left(1 - \frac{1}{\cosh[\phi_6 \cdot \max(0, Z_{1.0} - \phi_7)]}\right) + \frac{\phi_8}{\cosh[0.15 \cdot \max(0, Z_{1.0} - 15)]} \\
& + \eta_i + \varepsilon_{ij} \tag{13b}
\end{aligned}$$

The predictor variables for fixed effects are:

M	Moment magnitude
R_{RUP}	Closest distance to the rupture plane (km)
R_{JB}	Joyner-Boore distance to the rupture plane (km)
R_X	Site coordinate (km) measured perpendicular to the fault strike from the surface projection of the updip edge of the fault rupture, with the downdip direction being positive.
F_{HW}	Hanging-wall flag: 1 for $R_X \geq 0$ and 0 for $R_X < 0$
δ	Fault dip angle
Z_{TOR}	Depth to top of rupture (km)
F_{RV}	Reverse faulting flag: 1 for $30^\circ \leq \lambda \leq 150^\circ$ (combined reverse and reverse-oblique), 0 otherwise; λ is the rake angle.
F_{NM}	Normal faulting flag: 1 for $-120^\circ \leq \lambda \leq -60^\circ$ (excludes normal-oblique), 0 otherwise.
AS	Aftershock flag: 1 if the event is an aftershock, 0 otherwise
V_{S30}	Average shear wave velocity for top 30 m (m/s)
$Z_{1.0}$	Depth to shear wave velocity of 1.0 km/s (m).

The variability in ground motion is represented in Equations 13a and 13b by random variables η_i and ε_{ij} . The modeling of these variables using mixed-effects regression is discussed in the next section.

MIXED-EFFECTS MODEL FORMULATION AND VARIANCE MODEL INCORPORATING NONLINEAR SOIL RESPONSE

The coefficients of Equations 13a and 13b are developed using a mixed effects regression model (e.g., Brillinger and Preisler 1984; Abrahamson and Youngs 1992; Pinheiro and Bates 2000). The mixed effects model incorporates fixed effects to model the expected amplitude of $\ln(y)$ as a function of magnitude, distance, V_{S30} , etc, and random effects to represent a random shift of all observations for an individual earthquake from this expected amplitude. Just as fixed effects described in the previous section can be grouped into three components representing the physical processes of source, path, and site, the random errors in our model are divided into four independent components of source (η_i), path (ε_{Pij}), site (ε_{Sj}), and the remaining errors ε_{Xij} . The first component, η_i , is a random earthquake effect (Brillinger and Preisler 1984; Abrahamson and Youngs

1992). This random effect is attributed to the individual earthquake such that all recordings from the i^{th} earthquake deviate from the global population mean, μ , by a value η_i (also called the inter-event residual). The inter-event residuals are assumed to be independent and normally distributed with variance τ^2 .

Each of the three remaining error components is also assumed to be independent and normally distributed with a zero mean and variances σ_P^2 , σ_S^2 , and σ_X^2 , respectively. In practice, the remaining three components are often lumped into a combined intra-event residual ε_{ij} . Individual recording at station j from the i^{th} earthquake deviate from the earthquake-specific mean, $\mu + \eta_i$, by intra-event residuals, ε_{ij} , that are assumed to be normally distributed with variance σ^2 . In the following we show that due to nonlinear soil response the variance σ^2 is a function of soil nonlinearity.

Using Equation 10 and the geotechnical framework illustrated in Figure 11, the recorded motion, $\ln(y_{ij})$, is obtained by:

$$\ln(y_{ij}) = \ln(y_{ref_{ij}}) + \eta_i + \varepsilon_{Pij} + a_j + b_j \ln\left(\frac{e^{(\ln(y_{ref_{ij}}) + \eta_i + \varepsilon_{Pij}) + c}}}{c}\right) + \varepsilon_{Sj} + \varepsilon_{Xij} \quad (14)$$

where $y_{ref_{ij}}$ is the reference motion (specified by Equation 13a). The sum of $\ln(y_{ref_{ij}})$, the earthquake term η_i , and the path error ε_{Pij} (the first three terms of Equation 14) represents the logarithm of the incident motion to the soil column beneath a site. The level of this incident motion determines the average soil amplification factor. Note that the intra-event components ε_{Sj} and ε_{Xij} are not part of the incident motion and hence they do not affect the average soil amplification factor.

Though Equation 14 represents fully our conceptual model of ground motions, its use in regression analysis of empirical data is made difficult by the lack of repeatedly sampled paths and limited repeatedly sampled sites; and by the unavailability of an inference method capable of handling the complicated data structure induced by the path error ε_{Pij} being included as predictor of soil amplification. To get around these difficulties, we move ε_{Pij} outside of $\ln[(y_{ref_{ij}} e^{\eta_i + \varepsilon_{Pij}} + c)/c]$ by replacing the logarithm with the first two terms of its Taylor series expansion (a first-order approximation):

$$\ln(y_{ij}) = \ln(y_{ref_{ij}}) + \eta_i + \varepsilon_{Pij} + a_j + b_j \left(\ln\left(\frac{y_{ref_{ij}} e^{\eta_i + c}}{c}\right) + \frac{y_{ref_{ij}} e^{\eta_i}}{y_{ref_{ij}} e^{\eta_i + c}} \varepsilon_{Pij} \right) + \varepsilon_{Sj} + \varepsilon_{Xij} \quad (15)$$

Combining the error terms (not including η_i) into a single intra-event error ε_{ij} produces:

$$\varepsilon_{ij} = \varepsilon_{Pij} + \left[b_j \frac{y_{ref_{ij}} e^{\eta_i}}{y_{ref_{ij}} e^{\eta_i + c}} \right] \varepsilon_{Pij} + \varepsilon_{Sj} + \varepsilon_{Xij} \quad (16)$$

We now obtain the mixed-effects model used in our regression analysis:

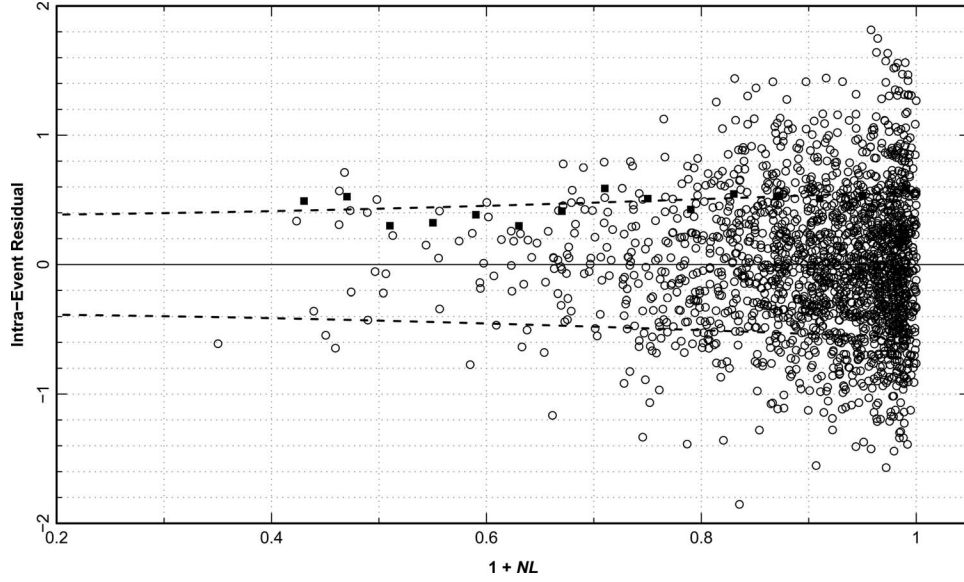


Figure 12. Intra-event residuals for 0.1-sec *PSA* plotted against the variance covariate ($1 + NL_{ij}$). The solid squares are bin estimates of standard deviation; the dashed lines show the fitted variance function.

$$\ln(y_{ij}) = \ln(y_{ref_{ij}}) + \eta_i + a_j + b_j \ln\left(\frac{y_{ref_{ij}} e^{\eta_i} + c}{c}\right) + \varepsilon_{ij} \quad (17)$$

In Equation 17 the effect of η_i on nonlinear soil de-amplification is still being carried exactly, but the effect of ε_{Pij} is (linearly) approximated and is now part of the intra-event error ε_{ij} , the 2nd term of Equation 16. The variance of the intra-event error ε_{ij} is given by:

$$\sigma^2 = \sigma_S^2 + \sigma_X^2 + \left(1 + b_j \frac{y_{ref_{ij}} e^{\eta_i}}{y_{ref_{ij}} e^{\eta_i} + c}\right)^2 \sigma_P^2 \quad (18)$$

It is important to note that the intra-event variance decreases with decreasing value of $[1 + b_j y_{ref_{ij}} e^{\eta_i} / (y_{ref_{ij}} e^{\eta_i} + c)]$. Therefore, the introduction of nonlinear site response into the ground motion prediction equation directly leads to heteroscedastic (non-constant) intra-event variance that is dependent on the response level. The variable $NL_{ij} = [b_j y_{ref_{ij}} e^{\eta_i} / (y_{ref_{ij}} e^{\eta_i} + c)]$, which is always less than or equal to 0 (the sign of b_j is negative), can be interpreted as a measure of soil nonlinearity affecting a strong-motion recording, with a value of 0 indicating linear response.

One way to explore the degree of intra-event heteroscedasticity in our NGA dataset is to plot intra-event residuals against $1 + NL_{ij}$. Intra-event residuals of $\ln(y_{ij})$ for a spectral period of 0.1 sec are plotted against $(1 + NL_{ij})$ in Figure 12. The quantities b_j , η_i , and

Table 1. Period-independent coefficients of model for $\ln(y_{ref})$ —Equation 13a

c_2	c_3	c_4	c_{4a}	c_{RB}	c_{HM}	$c_{\gamma 3}$
1.06	3.45	-2.1	-0.5	50	3	4

c needed for the calculation of NL_{ij} are taken from the fitted model for $T=0.1$ sec. To help see the variation of intra-event variance as a function of $(1+NL_{ij})$, intra-event standard errors computed for several non-overlapping intervals of $(1+NL_{ij})$ are plotted as solid squares. They clearly show a dependency of intra-event variance on $(1+NL_{ij})$ that is consistent with Equation 18. The dash curves plotted in Figure 12 shows the fitted variance model based on Equation 18.

MODEL DEVELOPMENT

ESTIMATION OF FIXED EFFECTS COEFFICIENTS

The fixed effects coefficients of the ground motion model (Equation 13a and 13b) were estimated using the nonlinear mixed effects method *nlme* (Pinheiro and Bates 2000) implemented in the statistical packages **S-PLUS** and **R**. The coefficients were developed through an iterative process of performing regressions for the entire spectral period range with some parts of the model fixed, developing smoothing models for these coefficients with period, and then repeating the analysis to examine the variation of the remaining coefficients. A full description of this iterative process can be found in Chiou and Youngs (2008).

All analyses were performed using the PEER-NGA data truncated at a maximum distance of $R_{RUP}=70$ km. The resulting coefficients are listed in Tables 1–3.

The estimated values of coefficient c_1 exhibited noticeable steps at periods of 0.8, 1.1, 1.6, 4, and 8 sec. These steps occur at spectral periods where there are large reductions in the number of usable data, defined by the record's minimum usable frequency (Chiou et al. 2008). This suggested that the estimated values of the model intercept may be biased by the systematic removal of weaker motions from the data set, which would tend to leave larger ground motion amplitudes in the remaining data. To correct this bias and to smooth c_1 , we imposed a smooth variation in the slope of c_1 with respect to period. Finally, we examined the shapes of displacement spectra for large magnitude earthquakes ($M \geq 6.5$) to verify that constant displacement is reached at spectral periods that are consistent with the model presented in BSSC (2004). The difference between the values of c_1 obtained from regression and the values reported after bias adjustment was incorporated into the assessment of the inter-event variance.

Table 2. Period-dependent coefficients of model for $\ln(y_{ref})$ —Equation 13a^a

Spectra Period (sec)	c_1	c_{1a}	c_{1b}	c_n	c_M	c_5	c_6	c_7	c_{7a}	c_9	c_{9a}	c_{10}	$c_{\gamma 1}$	$c_{\gamma 2}$
<i>pga</i>	-1.2687	0.1	-0.2550	2.996	4.1840	6.1600	0.4893	0.0512	0.0860	0.7900	1.5005	-0.3218	-0.00804	-0.00785
<i>pgv</i>	2.2884	0.1094	-0.0626	1.648	4.2979	5.1700	0.4407	0.0207	0.0437	0.3079	2.6690	-0.1166	-0.00275	-0.00625
0.01	-1.2687	0.1	-0.2550	2.996	4.1840	6.1600	0.4893	0.0512	0.0860	0.7900	1.5005	-0.3218	-0.00804	-0.00785
0.02	-1.2515	0.1	-0.2550	3.292	4.1879	6.1580	0.4892	0.0512	0.0860	0.8129	1.5028	-0.3323	-0.00811	-0.00792
0.03	-1.1744	0.1	-0.2550	3.514	4.1556	6.1550	0.4890	0.0511	0.0860	0.8439	1.5071	-0.3394	-0.00839	-0.00819
0.04	-1.0671	0.1	-0.2550	3.563	4.1226	6.1508	0.4888	0.0508	0.0860	0.8740	1.5138	-0.3453	-0.00875	-0.00855
0.05	-0.9464	0.1	-0.2550	3.547	4.1011	6.1441	0.4884	0.0504	0.0860	0.8996	1.5230	-0.3502	-0.00912	-0.00891
0.075	-0.7051	0.1	-0.2540	3.448	4.0860	6.1200	0.4872	0.0495	0.0860	0.9442	1.5597	-0.3579	-0.00973	-0.00950
0.1	-0.5747	0.1	-0.2530	3.312	4.1030	6.0850	0.4854	0.0489	0.0860	0.9677	1.6104	-0.3604	-0.00975	-0.00952
0.15	-0.5309	0.1	-0.2500	3.044	4.1717	5.9871	0.4808	0.0479	0.0860	0.9660	1.7549	-0.3565	-0.00883	-0.00862
0.2	-0.6352	0.1	-0.2449	2.831	4.2476	5.8699	0.4755	0.0471	0.0860	0.9334	1.9157	-0.3470	-0.00778	-0.00759
0.25	-0.7766	0.1	-0.2382	2.658	4.3184	5.7547	0.4706	0.0464	0.0860	0.8946	2.0709	-0.3379	-0.00688	-0.00671
0.3	-0.9278	0.0999	-0.2313	2.505	4.3844	5.6527	0.4665	0.0458	0.0860	0.8590	2.2005	-0.3314	-0.00612	-0.00598
0.4	-1.2176	0.0997	-0.2146	2.261	4.4979	5.4997	0.4607	0.0445	0.0850	0.8019	2.3886	-0.3256	-0.00498	-0.00486
0.5	-1.4695	0.0991	-0.1972	2.087	4.5881	5.4029	0.4571	0.0429	0.0830	0.7578	2.5000	-0.3189	-0.00420	-0.00410
0.75	-1.9278	0.0936	-0.1620	1.812	4.7571	5.2900	0.4531	0.0387	0.0690	0.6788	2.6224	-0.2702	-0.00308	-0.00301
1	-2.2453	0.0766	-0.1400	1.648	4.8820	5.2480	0.4517	0.0350	0.0450	0.6196	2.6690	-0.2059	-0.00246	-0.00241
1.5	-2.7307	0.0022	-0.1184	1.511	5.0697	5.2194	0.4507	0.0280	0.0134	0.5101	2.6985	-0.0852	-0.00180	-0.00176
2	-3.1413	-0.0591	-0.1100	1.470	5.2173	5.2099	0.4504	0.0213	0.0040	0.3917	2.7085	0.0160	-0.00147	-0.00143
3	-3.7413	-0.0931	-0.1040	1.456	5.4385	5.2040	0.4501	0.0106	0.0010	0.1244	2.7145	0.1876	-0.00117	-0.00115
4	-4.1814	-0.0982	-0.1020	1.465	5.5977	5.2020	0.4501	0.0041	0	0.0086	2.7164	0.3378	-0.00107	-0.00104
5	-4.5187	-0.0994	-0.1010	1.478	5.7276	5.2010	0.4500	0.0010	0	0	2.7172	0.4579	-0.00102	-0.00099
7.5	-5.1224	-0.0999	-0.1010	1.498	5.9891	5.2000	0.4500	0	0	0	2.7177	0.7514	-0.00096	-0.00094
10	-5.5872	-0.1	-0.1000	1.502	6.1930	5.2000	0.4500	0	0	0	2.7180	1.1856	-0.00094	-0.00091

^a Units are g's for *pga* and *psa*, and cm/sec for *pgv*

Table 3. Coefficients of site response model for $\ln(y)$ —Equation 13b

Spectra Period (sec)	φ_1	φ_2	φ_3	φ_4	φ_5	φ_6	φ_7	φ_8
<i>pga</i>	-0.4417	-0.1417	-0.007010	0.102151	0.2289	0.014996	580.0	0.0700
<i>pgv</i>	-0.7861	-0.0699	-0.008444	5.41000	0.2899	0.006718	459.0	0.1138
0.01	-0.4417	-0.1417	-0.007010	0.102151	0.2289	0.014996	580.0	0.0700
0.02	-0.4340	-0.1364	-0.007279	0.108360	0.2289	0.014996	580.0	0.0699
0.03	-0.4177	-0.1403	-0.007354	0.119888	0.2289	0.014996	580.0	0.0701
0.04	-0.4000	-0.1591	-0.006977	0.133641	0.2289	0.014996	579.9	0.0702
0.05	-0.3903	-0.1862	-0.006467	0.148927	0.2290	0.014996	579.9	0.0701
0.075	-0.4040	-0.2538	-0.005734	0.190596	0.2292	0.014996	579.6	0.0686
0.1	-0.4423	-0.2943	-0.005604	0.230662	0.2297	0.014996	579.2	0.0646
0.15	-0.5162	-0.3113	-0.005845	0.266468	0.2326	0.014988	577.2	0.0494
0.2	-0.5697	-0.2927	-0.006141	0.255253	0.2386	0.014964	573.9	-0.0019
0.25	-0.6109	-0.2662	-0.006439	0.231541	0.2497	0.014881	568.5	-0.0479
0.3	-0.6444	-0.2405	-0.006704	0.207277	0.2674	0.014639	560.5	-0.0756
0.4	-0.6931	-0.1975	-0.007125	0.165464	0.3120	0.013493	540.0	-0.0960
0.5	-0.7246	-0.1633	-0.007435	0.133828	0.3610	0.011133	512.9	-0.0998
0.75	-0.7708	-0.1028	-0.008120	0.085153	0.4353	0.006739	441.9	-0.0765
1	-0.7990	-0.0699	-0.008444	0.058595	0.4629	0.005749	391.8	-0.0412
1.5	-0.8382	-0.0425	-0.007707	0.031787	0.4756	0.005544	348.1	0.0140
2	-0.8663	-0.0302	-0.004792	0.019716	0.4785	0.005521	332.5	0.0544
3	-0.9032	-0.0129	-0.001828	0.009643	0.4796	0.005517	324.1	0.1232
4	-0.9231	-0.0016	-0.001523	0.005379	0.4799	0.005517	321.7	0.1859
5	-0.9222	0.0000	-0.001440	0.003223	0.4799	0.005517	320.9	0.2295
7.5	-0.8346	0.0000	-0.001369	0.001134	0.4800	0.005517	320.3	0.2660
10	-0.7332	0.0000	-0.001361	0.000515	0.4800	0.005517	320.1	0.2682

RESIDUALS

Figure 13 shows the inter-event residuals, η_i , for main shocks. The residuals do not exhibit a trend with magnitude. The values for California and non-California earthquakes do not show any trends with respect to the population mean, indicating that both sets of earthquakes are consistent with the model. These results indicate that the data from the other active tectonic regions are consistent with ground motions from California earthquakes. The inter-event term for the Chi-Chi main shock is approximately $2 \times \tau$ below the population mean for *pga* (0.01 sec spectral acceleration), and becomes positive for periods longer than 1.0 sec.

Figures 14–17 show the intra-event residuals plotted versus \mathbf{M} , R_{RUP} , V_{S30} , and y_{ref} for spectral periods of 0.01 (*pga*), 0.2, 1.0 and 3.0 sec, respectively. The residuals do not exhibit any trends with respect to \mathbf{M} , R_{RUP} , V_{S30} , or y_{ref} . The site response model we have developed (Equation 10) assumes that there is no deamplification of ground motions relative to y_{ref} for sites with V_{S30} greater than 1130 m/sec. Although there is very

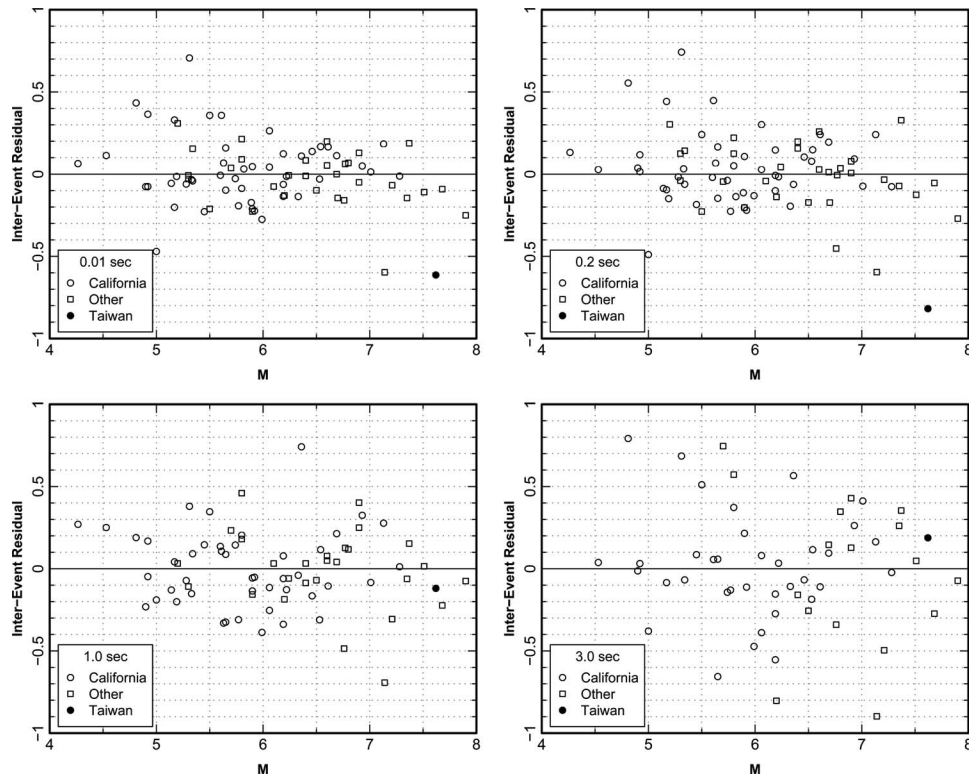


Figure 13. Mainshock inter-event residuals for spectral periods of 0.01 sec (*pga*), 0.2, 1.0 and 3.0 seconds.

little data in the PEER-NGA data base for such sites, the limited data, if anything, suggest a slight upward trend in the residuals. The site amplification model developed here does not account for the effect of the lower kappa expected for hard rock sites which would lead to increases in high frequency ground motions.

Figure 18 shows intra-event residuals plotted against R_{RUP} for the 10 earthquakes in the NGA database for which we developed extended *pga* data sets. The intra-event residuals are computed using the inter-event residual for each earthquake computed from just the NGA data within 70 km as part of our overall fit to the NGA. These results show that the model provides a good fit at distances greater than 70 km. Also shown is the bias in the NGA data set at larger distances.

VARIANCE MODEL

During the first stages of model development, the results suggested that the standard error terms did not depend upon earthquake magnitude in contrast to the previous Sadigh et al. (1997) models. This was based on visual inspection of the residuals. However, statistical analysis of the residuals indicated that a statistically significant dependence on

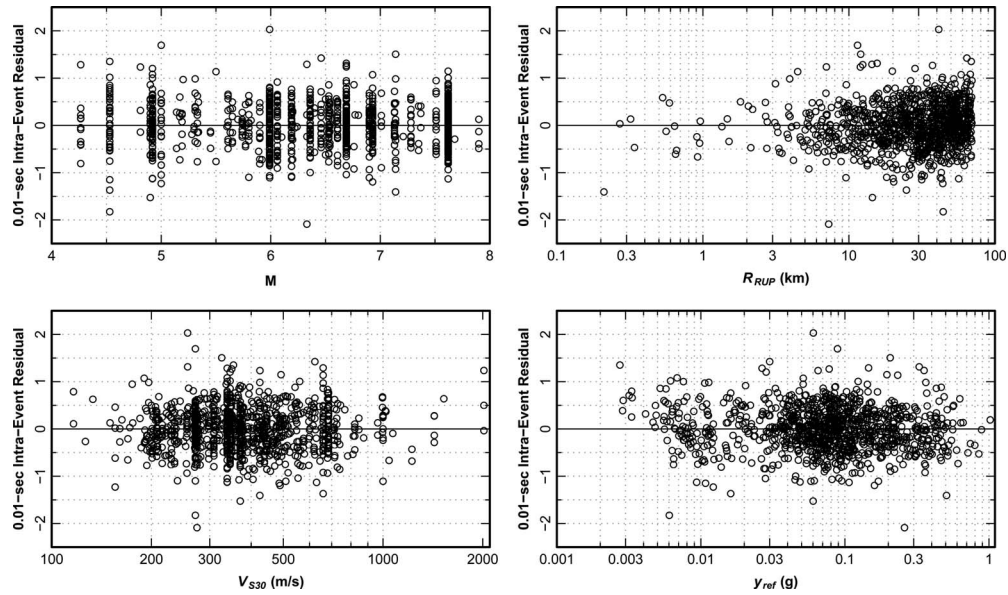


Figure 14. Intra-event residuals for spectral period of 0.01 sec (pga) plotted against M , R_{RUP} , V_{S30} , and y_{ref} .

magnitude is present, although the amplitude of the effect is less than found by Sadigh et al. (1997). The statistical test employed followed that used by Youngs et al. (1995). We first computed the log-likelihood for the model assuming magnitude-independent variance terms, then using the tri-linear model for magnitude-dependent variance used by Youngs et al. (1995). We then used the likelihood ratio test to check the significance of the increase in log-likelihood found assuming magnitude-dependent variance. Magnitude-dependence in the variance terms was found to be statistically significant (p -values < 0.05) for periods up to about 1 second. For longer periods the results showed less statistical significance, but at the same time there is a large reduction in the size of the data set, particularly in data from smaller magnitude earthquakes.

We performed two additional checks on possible contributions to the observed magnitude-dependence. We found that value of the intra-event standard deviation for the aftershock data is approximately 0.08 larger than that for the main shock data. When this was accounted for in the variance model, magnitude-dependence in the mainshock residuals was still found to be statistically significant. Similar estimates of inter-event variability were obtained for main shocks and aftershocks. Secondly, the reduction in intra-event variance due to nonlinear soil response could also contribute to the observed magnitude-dependence as larger earthquakes tend to produce larger motions, and thus induce greater nonlinear response. This effect was explored by Youngs et al. (1995), who found that it was not a major contributing factor. We tested the influence of soil nonlinearity by comparing the log-likelihoods obtained for data sets restricted to nonlinearity factors $NL > -0.15$ and again found that magnitude-dependence of the variance terms is

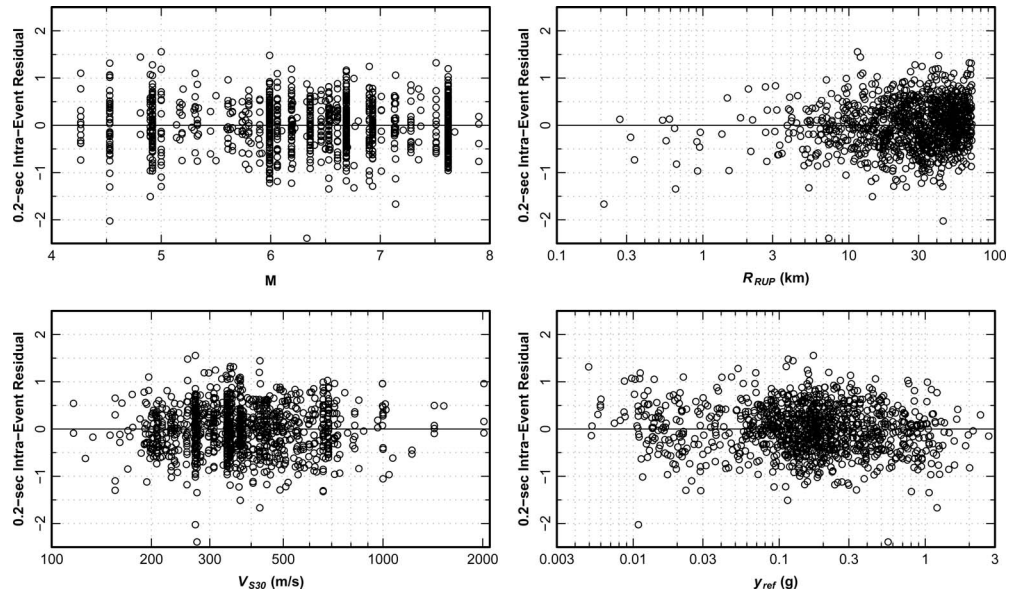


Figure 15. Intra-event residuals for spectral period of 0.2 sec plotted against M , R_{RUP} , V_{S30} , and y_{ref}

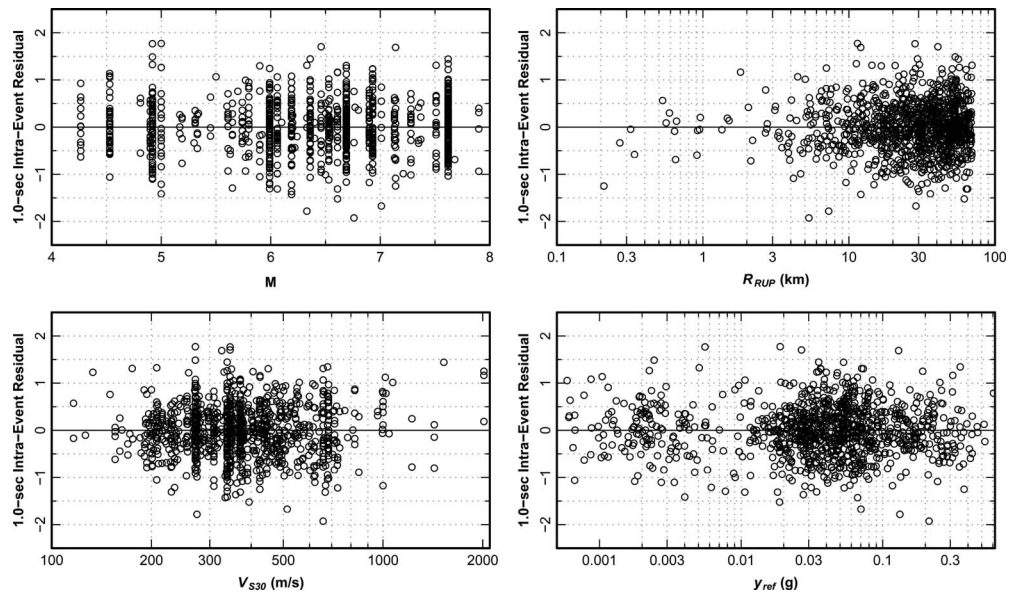


Figure 16. Intra-event residuals for spectral period of 1.0 sec plotted against M , R_{RUP} , V_{S30} , and y_{ref}

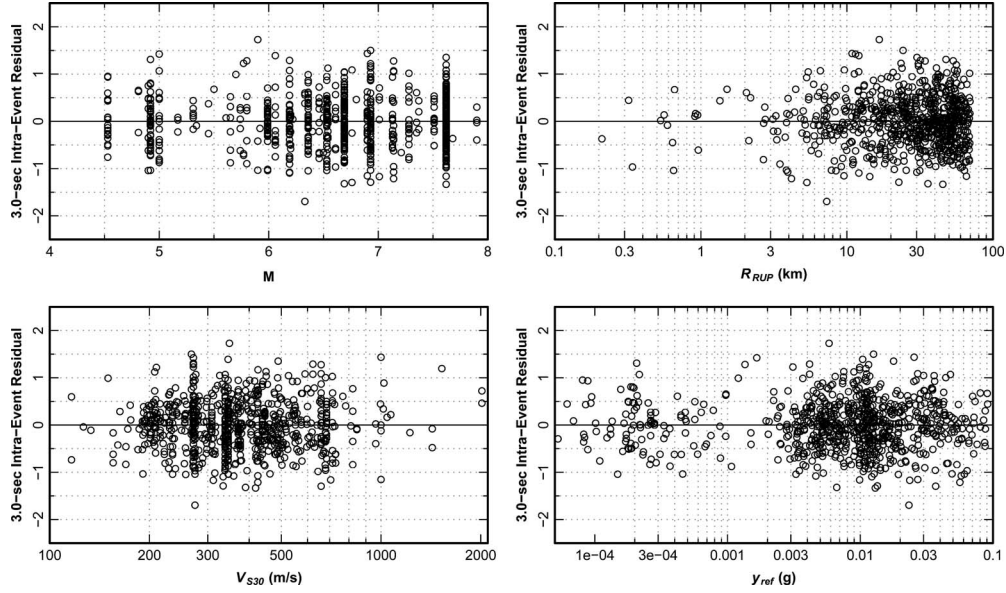


Figure 17. Intra-event residuals for spectral period of 3.0 sec plotted against M , R_{RUP} , V_{S30} , and y_{ref}

statistically significant over much of the period range. Restricting the degree of nonlinearity further to $NL > -0.05$ resulted in greatly reducing the size of the data set to the level where there is large uncertainty in estimating the variance terms.

The model for the inter-event standard error τ is given by:

$$\tau = \tau_1 + \frac{\tau_2 - \tau_1}{2} \times [\min\{\max(M, 5), 7\} - 5] \quad (19)$$

The smoothed values of τ_1 and τ_2 are listed in Table 4. Magnitude-dependence in τ is much weaker than was estimated in the Sadigh et al. (1997) models and disappears for periods longer than 2 seconds. The inter-event residuals also display increased variability near a spectral period of 0.1 seconds compared to larger and smaller periods.

The intra-event residuals display stronger magnitude dependence than the inter-event residuals. The variability is also affected by the degree of nonlinearity in the soil, as defined by Equation 18. In addition, greater variability is observed in the residuals for sites with inferred values of V_{S30} than for sites with measured values of V_{S30} . The model for the intra-event standard deviation that incorporates these observations is given by:

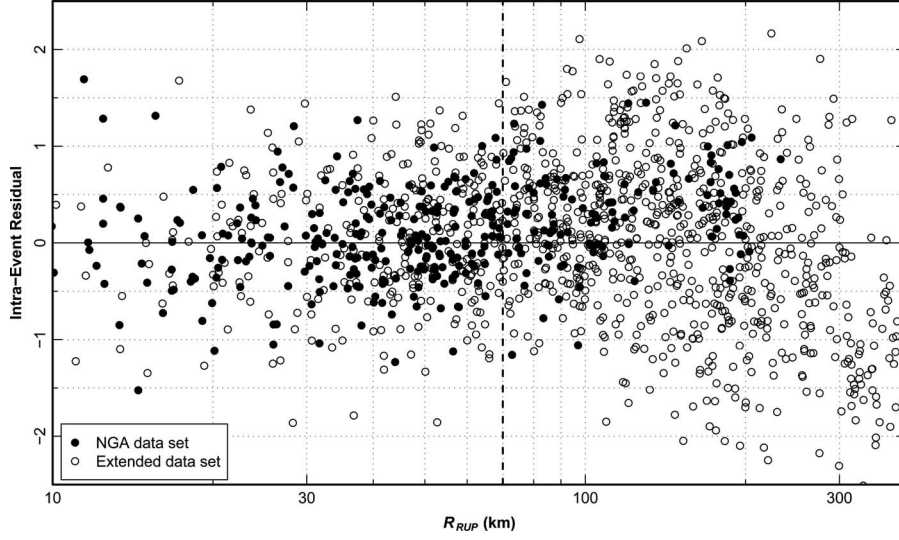


Figure 18. Intra-event residuals for pga for the 1994 Northridge, 1998 San Juan Bautista, 1999 Hector Mines, 2000 Yountville, 2001 Mohawk Valley, 2001 Anza, 2002 Baja, 2002 Gilroy, 2002 Yorba Linda, and 2003 Big Bear City earthquakes.

$$\sigma = \left[\sigma_1 + \frac{\sigma_2 - \sigma_1}{2} (\min\{\max(\mathbf{M}, 5), 7\} - 5) + \sigma_4 \times AS \right] \times \sqrt{(\sigma_3 F_{Inferred} + 0.7 F_{Measured}) + (1 + NL)^2} \quad (20)$$

with

$$NL = \left(b \frac{y_{ref} e^\eta}{y_{ref} e^\eta + c} \right),$$

where $F_{Inferred}$ equals 1, if V_{S30} is inferred from geology, and 0 otherwise; $F_{Measured}$ equals 1, if V_{S30} is measured, and 0 otherwise; and AS equals 1 if the event is an after-shock, and 0 otherwise. Coefficients σ_1 , σ_2 , σ_3 , and σ_4 are listed in Table 4.

The total variance for $\ln(y)$ is the sum of the inter-event and intra-event variances. Based on Equation 20, the intra-event variance is a function of the random effect η such that calculation of the total variance σ_T^2 requires integration over the random effects. We provide an approximate method that does not require integration. Taking the first order approximation of the Taylor series expansion for σ_T^2 evaluated at $\eta=0$ yields the expression:

$$\sigma_T^2 = (1 + NL_0)^2 \tau^2 + \sigma_{NL_0}^2 \quad (21)$$

with

Table 4. Coefficients of variance model—Equations 19 and 20

Spectra Period (sec)	τ_1	τ_2	σ_1	σ_2	σ_3	σ_4
<i>pga</i>	0.3437	0.2637	0.4458	0.3459	0.8	0.0663
<i>pgv</i>	0.2539	0.2381	0.4496	0.3554	0.7504	0.0133
0.01	0.3437	0.2637	0.4458	0.3459	0.8	0.0663
0.02	0.3471	0.2671	0.4458	0.3459	0.8	0.0663
0.03	0.3603	0.2803	0.4535	0.3537	0.8	0.0663
0.04	0.3718	0.2918	0.4589	0.3592	0.8	0.0663
0.05	0.3848	0.3048	0.4630	0.3635	0.8	0.0663
0.075	0.3878	0.3129	0.4702	0.3713	0.8	0.0663
0.1	0.3835	0.3152	0.4747	0.3769	0.8	0.0663
0.15	0.3719	0.3128	0.4798	0.3847	0.8	0.0612
0.2	0.3601	0.3076	0.4816	0.3902	0.8	0.0530
0.25	0.3522	0.3047	0.4815	0.3946	0.7999	0.0457
0.3	0.3438	0.3005	0.4801	0.3981	0.7997	0.0398
0.4	0.3351	0.2984	0.4758	0.4036	0.7988	0.0312
0.5	0.3353	0.3036	0.4710	0.4079	0.7966	0.0255
0.75	0.3429	0.3205	0.4621	0.4157	0.7792	0.0175
1	0.3577	0.3419	0.4581	0.4213	0.7504	0.0133
1.5	0.3769	0.3703	0.4493	0.4213	0.7136	0.0090
2	0.4023	0.4023	0.4459	0.4213	0.7035	0.0068
3	0.4406	0.4406	0.4433	0.4213	0.7006	0.0045
4	0.4784	0.4784	0.4424	0.4213	0.7001	0.0034
5	0.5074	0.5074	0.4420	0.4213	0.7000	0.0027
7.5	0.5328	0.5328	0.4416	0.4213	0.7000	0.0018
10	0.5542	0.5542	0.4414	0.4213	0.7000	0.0014

$$NL_0 = \left(b \frac{y_{ref}}{y_{ref} + c} \right)$$

In Equation 21 τ is obtained from Equation 19, and $\sigma_{NL_0}^2$ is evaluated using Equation 20 with $\eta=0$. We evaluated the performance of Equation 21 compared to numerical integration over η and to Monte-Carlo simulation and found that it produces results that are, in most cases, within a few percent of the more exact calculations, with the values obtained from Equation 21 slightly larger than the exact solution. Therefore, we recommend the use of Equation 21 for calculating the total variance of $\ln(y)$ about the population mean given by Equations 13a and 13b.

MODEL COMPARISONS

Figures 19–21 compare magnitude and distance scaling produced by the new model with that predicted by the models developed by Sadigh et al. (1997). The comparisons require an assessment of V_{S30} representative of the Sadigh et al. (1997) relationships. For

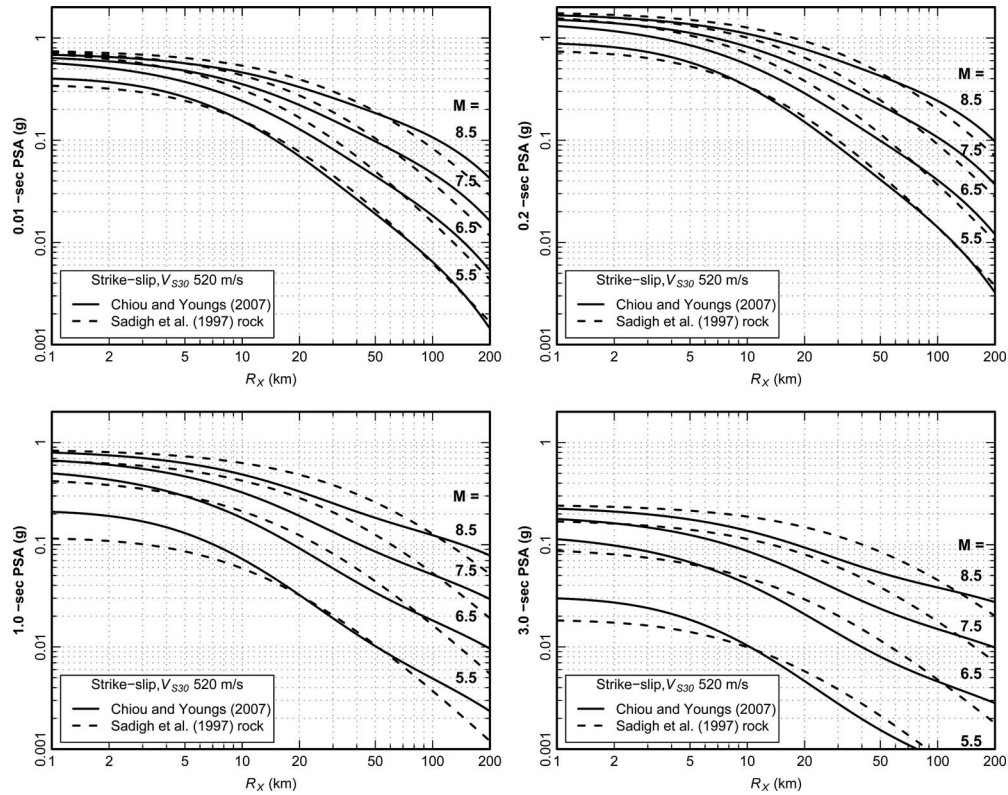


Figure 19. Magnitude and distance scaling predicted by the model developed in this study and predicted by Sadigh et al. (1997) for horizontal distance from a vertical strike-slip fault and soft rock sites.

soil, we have used a value of 310 m/s, the velocity suggested by Boore et al. (1997) as representative of generic soil. This value is also approximately the geometric mean of V_{S30} for sites in the PEER-NGA database that would have been included in the Sadigh et al. (1997) soil database. For generic rock, Boore et al. (1997) suggested a value of 620 m/s. However, we think that this may be higher than the average for the data used by Sadigh et al. (1997), which included recordings from many sites that are now classified as NEHRP C, and have used a V_{S30} of 520 m/s for the comparisons.

The bulk of the ground motion data are for soil sites and at distances between 20 and 50 km and the two models produce generally similar results for these conditions and short period motions. The models are more similar for soil than for rock, which is to be expected given that the majority of ground motion data is recorded on soil sites. The difference between the two models increases for longer period motions, with the new model generally indicating lower motions. This difference is attributed largely to the much larger spectral acceleration database available to constrain the model coefficients compared to the amount of data available for use by the Sadigh et al. (1997). Differences

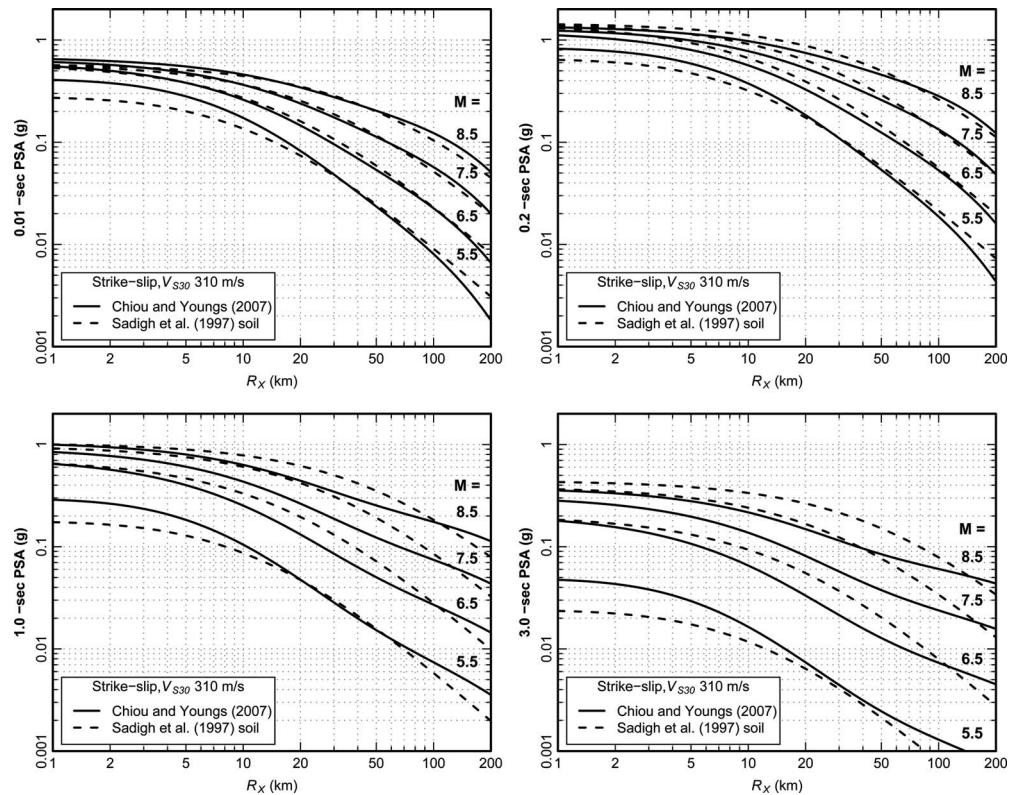


Figure 20. Magnitude and distance scaling predicted by the model developed in this study and predicted by Sadigh et al. (1997) for horizontal distance from a vertical strike-slip fault and firm soil sites.

in the model formulations account for the differences in predicted ground motions at the edges of the data. The distance scaling formulations are quite different, resulting in differences in the shape of the attenuation curves beyond 70 km, especially for long period motions. The introduction of the hanging-wall effect results in increases in the model predictions over those of Sadigh et al. (1997) for sites located in the hanging wall and reductions at other sites. The style of faulting effect for reverse earthquakes is now smaller and reduces with increasing spectral period. Differences in the predictions also occur for smaller magnitudes at close distances due to the revised scaling formulations.

Figures 22 and 23 compare median response spectra for the two models. The spectral shapes generated by the two models are similar, but as indicated in Figures 19–21, the updated model produces lower long period motions.

Figure 24, part (a) compares the total standard errors for the updated model with linear soil response compared to those for the Sadigh et al. (1997) models. The total

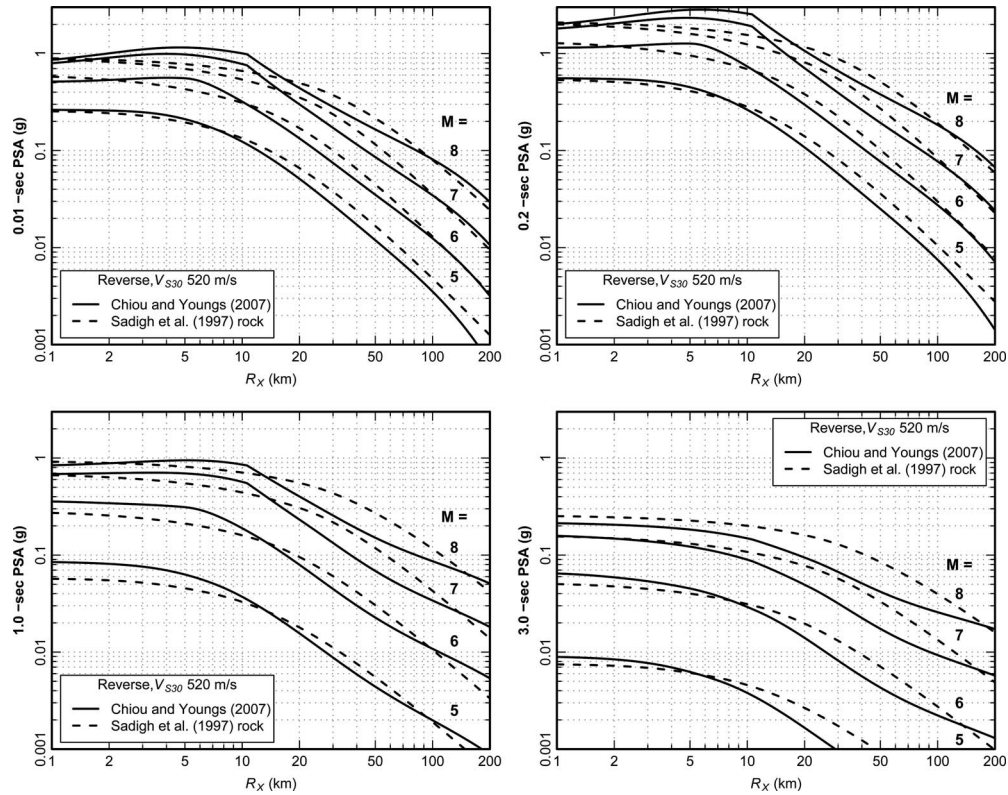


Figure 21. Magnitude and distance scaling predicted by the model developed in this study and predicted by Sadigh et al. (1997) for horizontal distance from the top edge of rupture on a reverse fault ($\delta=45^\circ$) and soft rock sites.

standard errors for **M** 5 earthquakes are similar but the updated standard errors for **M** 7 earthquakes are larger. Part (b) of the figure shows the effect of soil nonlinearity on the total standard errors of *pga*.

MODEL APPLICABILITY

The model developed in this study is considered to be applicable for estimating pseudo spectral accelerations (5% damping) and peak motions for earthquakes in active tectonic regions in which the following conditions apply:

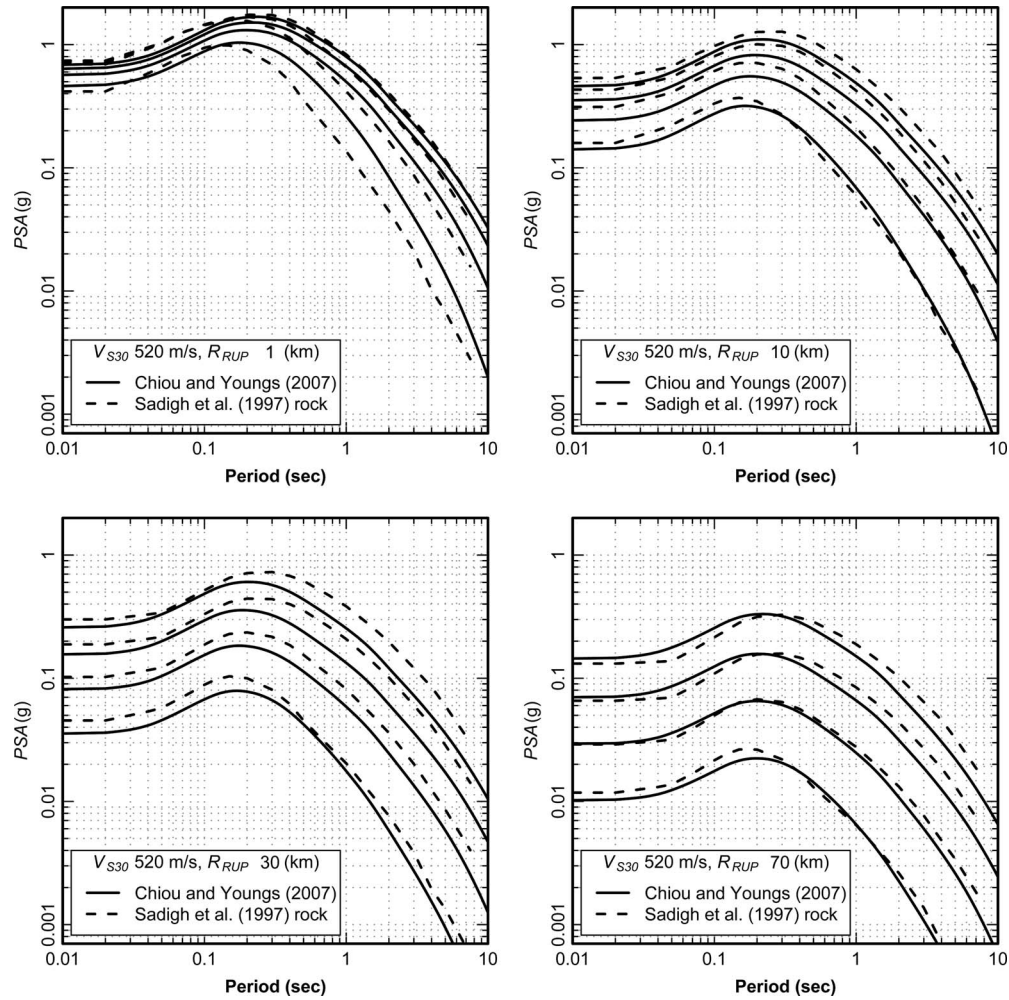


Figure 22. Median response spectra predicted by the model developed in this study and predicted by Sadigh et al. (1997) strike slip earthquakes and soft rock sites. Magnitudes are in order of increasing amplitude M 5.5, 6.5, 7.5, and 8.5.

- $4 \leq M \leq 8.5$ for strike-slip earthquakes
- $4 \leq M \leq 8.0$ for reverse and normal faulting earthquakes
- $0 \leq R_{RUP} \leq 200$ km
- $150 \text{ m/sec} \leq V_{S30} \leq 1500 \text{ m/sec}$.

The model was developed using the anelastic attenuation coefficient γ constrained by data from California earthquakes. For application in other regions where earthquakes at distances greater than about 50 km are a major contributor to the hazard, adjustments to the γ coefficients c_{γ_1} and c_{γ_2} may be warranted. These adjustments can be made using

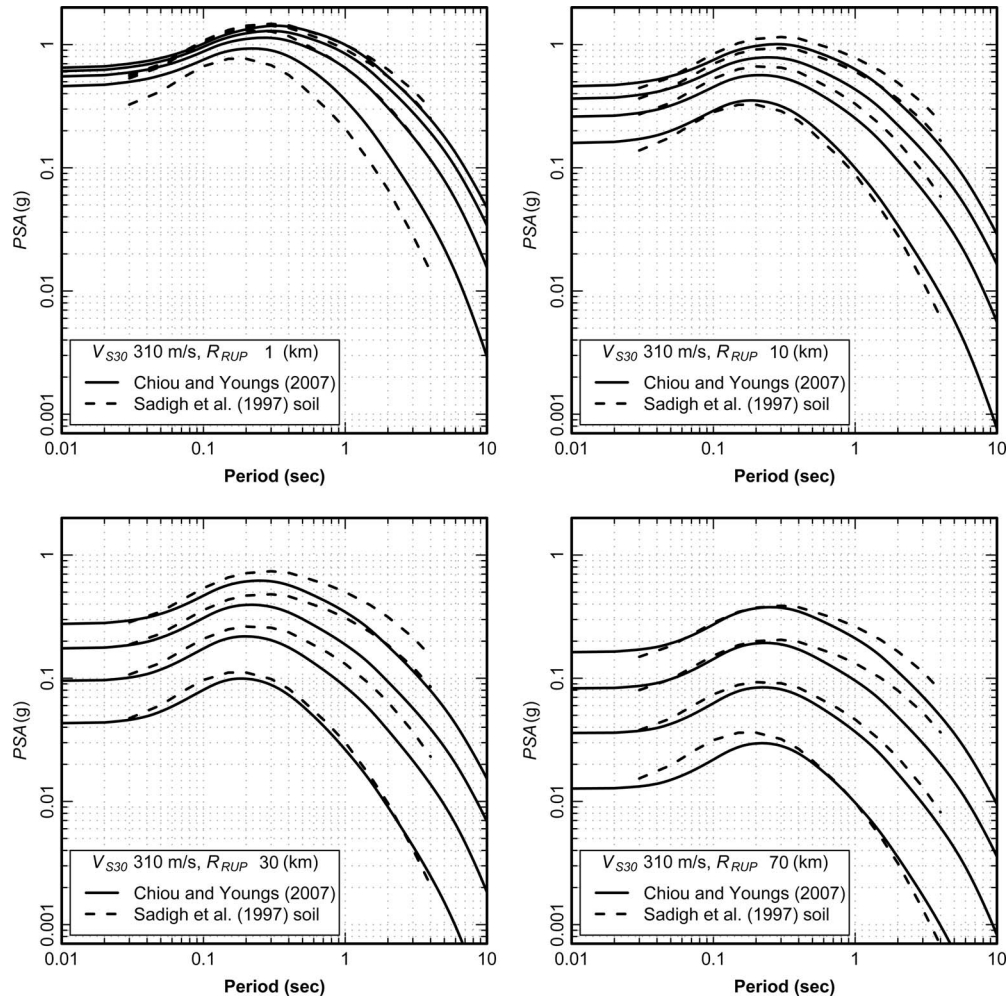


Figure 23. Median response spectra predicted by the model developed in this study and predicted by Sadigh et al. (1997) strike slip earthquakes and firm soil sites. Magnitudes are in order of increasing amplitude M 5.5, 6.5, 7.5, and 8.5.

the hybrid approach developed by Campbell (2003). In making such adjustments, we stress the need for the user to obtain estimates of Q for the two regions that are based on consistent geometric spreading models.

The site response portion of the ground motion model was constrained such that all ground motion amplification factors are 1 for V_{S30} greater than 1130 m/s. As the rock velocity increases we expect shallow crustal damping (i.e., “kappa”) to decrease, resulting in increases in high frequency motion. Data for such sites are not present in the

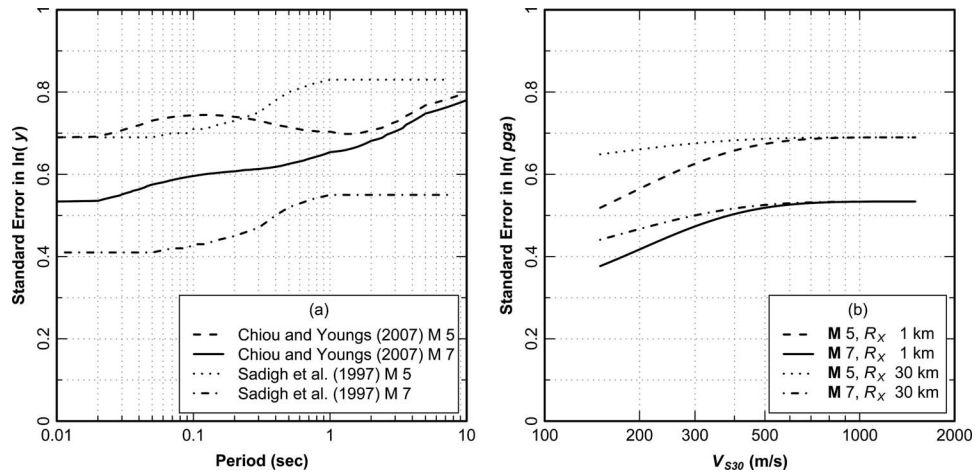


Figure 24. (a) Total standard errors for the model with linear site response developed in this study and Sadigh et al. (1997). (b) Effect of soil nonlinearity on *pga* total standard error for the model developed in this study.

PEER-NGA database in sufficient quantity to estimate this effect and it is not captured in our model. Such effects should be considered if the model is to be applied to sites with V_{S30} greater than 1500 m/sec.

The model was developed using recordings from earthquakes with a maximum depth to top of rupture of 15 km and a maximum hypocentral depth of 19 km. The model predicts a linear increase in $\ln(\gamma_{ref})$ with increasing Z_{TOR} over this range for most spectral periods. Application of the model in regions with very thick crust (e.g., ≥ 20 km) is an extrapolation outside of the range of data used to develop the model coefficients.

The ground motion model presented here is sensitive to the value of sediment depth, $Z_{1,0}$, for the site. We have used data from the SCEC-3D Version 4 model for southern California and users should use this version to estimate values of $Z_{1,0}$ at sites in southern California. For general application, we recommend that the user estimate $Z_{1,0}$ from Equation 1 unless there is site-specific data to provide a better estimate (e.g., a site velocity profile). Note also that large values of $Z_{1,0}$ may produce numerical overflow of the *cosh* function in some compilers and the user may need to determine the appropriate limits in implementing our model in computer programs.

ACKNOWLEDGMENTS

This study was sponsored by PEER Center's Program of Applied Earthquake Engineering Research of Lifelines Systems supported by the California Department of Transportation, the California Energy Commission, and the Pacific Gas & Electric Company. This work made use of the Earthquake Engineering Research Centers Shared Facilities supported by the National Science Foundation under award number EEC-9701568 through the PEER Center. Any opinions, findings, and conclusion or recommendations expressed in this material are those of the authors and do not necessarily reflect those of the National Science Foundation. The authors wish to thank Dr. Arthur Frankel and an anonymous reviewer for many helpful comments and suggestions that greatly improved this manuscript. We also wish to thank all of the members of the PEER-NGA project for many enlightening interactions. The graphics in this paper were prepared using **R** (R Development Core Team, 2006).

REFERENCES

- Abrahamson, N. A., and Silva, W. J., 1997. Empirical response spectral attenuation relations for shallow crustal earthquakes, *Seismol. Res. Lett.* **68**, 94–127.
- Abrahamson, N. A., and Somerville, P. G., 1996. Effects of the hanging wall and footwall on the ground motions recorded during the Northridge earthquake, *Bull. Seismol. Soc. Am.* **86**, S93–S99.
- Abrahamson, N. A., and Youngs, R. R., 1992. A stable algorithm for regression analyses using the random effects model, *Bull. Seismol. Soc. Am.* **82**, 505–510.
- Ambraseys, N. N., Douglas, J., Sarmal, S. K., and Smit, P. M., 2005. Equations for the estimation of strong ground motions from shallow crustal earthquakes using data from Europe and the Middle East: Horizontal peak ground acceleration and spectral acceleration, *Bulletin of Earthquake Engineering* **3**, 1–35.
- BSSC, 2004. *NEHRP Recommended Provisions for Seismic Regulations for New Buildings and Other Structures*, 2003 Edition, FEMA Publication 450, Building Seismic Safety Council, Washington, D.C.
- Atkinson, G. M., 1989. Attenuation of the Lg phase and site response for the Eastern Canada Telemetered Network, *Seismol. Res. Lett.* **60** (2), 59–69.
- Atkinson, G. M., and Mereu, R., 1992. The shape of ground motion attenuation curves in southeastern Canada, *Bull. Seismol. Soc. Am.* **82**, 2014–2031.
- Atkinson, G. M., and Silva, W., 1997. An empirical study of earthquake source spectra for California earthquakes, *Bull. Seismol. Soc. Am.* **87**, 97–113.
- , 2000. Stochastic modeling of California ground motions, *Bull. Seismol. Soc. Am.* **90**, 255–274.
- Bazzurro, P., and Cornell, C. A., 2004. Ground-motion amplification in nonlinear soil sites with uncertain properties, *Bull. Seismol. Soc. Am.* **94**, 2090–2109.
- Boatwright, J., Bundock, H., Luetgert, J., Seekins, L., Gee, L., and Lombard, P., 2003. The dependence of PGA and PGV on distance and magnitude inferred from northern California ShakeMap data, *Bull. Seismol. Soc. Am.* **93**, 2043–2055.

- Boatwright, J., Blair, L., Catchings, R., Goldman, M., Perosi, F., and Steedman, C., 2004. *Using Twelve Years of USGS Refraction Lines to Calibrate the Brocher and Others (1997) 3D Velocity Model of the Bay Area*, U.S. Geological Survey Open File Report 2004-1282.
- Boore, D. M., 2003. Simulation of ground motion using the stochastic method, *PAGEOPH* **160**, 635-676.
- Boore, D. M., and Joyner, W. B., 1997. Site amplification for generic rock sites, *Bull. Seismol. Soc. Am.* **87**, 327-341.
- Boore, D. M., Joyner, W. B., and Fumal, T. E., 1993. *Estimation of response spectra and peak accelerations from western North American earthquakes: An interim report*, U.S. Geological Survey Open-File Report 93-509, 72 pp.
- , 1997. Equations for estimating horizontal response spectra and peak acceleration from western North American earthquakes—A summary of recent work, *Seismol. Res. Lett.* **68**, 128-153.
- Boore, D. M., Watson-Lamprey, J., and Abrahamson, N. A., 2006. GMRotD and GMRotI: Orientation-independent measures of ground motion *Bull. Seismol. Soc. Am.* **96**, 1202-1511.
- Bragato, P. L., 2004. Regression analysis with truncated samples and its application to ground-motion attenuation studies, *Bull. Seismol. Soc. Am.* **94**, 1369-1378.
- Brillinger, D. R., and Preisler, H. K., 1984. An exploratory analysis of the Joyner-Boore attenuation data, *Bull. Seismol. Soc. Am.* **74**, 1441-1450.
- Campbell, K. W., 1989. *Empirical Prediction of Near-source Ground Motion for the Diablo Canyon Power Plant Site*, San Luis Obispo County, California, U.S. Geological Survey Open-File Report 89-484.
- , 1993. Empirical prediction of near-source ground motion from large earthquakes, *Proceedings International Workshop on Earthquake Hazards and Large Dams in the Himalaya*, January 15-16, New Delhi, India.
- , 2003. Prediction of strong ground motion using the hybrid empirical method and its use in the development of ground motion (attenuation) relations in eastern North America, *Bull. Seismol. Soc. Am.* **93**, 1012-1033.
- Campbell, K. W., and Bozorgnia, Y., 2003. Updated near-source ground-motion (attenuation) relations for the horizontal and vertical components of peak ground acceleration and acceleration response spectra, *Bull. Seismol. Soc. Am.* **93**, 314-331.
- Chiou, B. S.-J., Darragh, R., Gregor, N., and Silva, W., 2008. NGA project strong-motion database, *Earthquake Spectra* **24**, 23-44.
- Chiou, B. S.-J., and Youngs, R. R., 2008. Chiou and Youngs PEER-NGA empirical ground motion model for the average horizontal component of peak acceleration, peak velocity, and pseudo-spectral acceleration for spectral periods of 0.01 to 10 seconds, Final Report submitted to PEER.
- Chiou, B. S.-J., Makdisi, F. I., and Youngs, R. R., 2000. *Style-of-Faulting and Footwall/Hanging Wall Effects on Strong Ground Motion*, FY 1995 NEHRP Award Number 1434-95-G-2614, final report, 21 pp.
- Choi, Y., and Stewart, J. P., 2005. Nonlinear site amplification as function of 30 m shear wave velocity, *Earthquake Spectra* **21**, 1-30.
- Choi, Y., Stewart, J. P., and Graves, R. W., 2005. Empirical model for basin effect accounting for basin depth and source location, *Bull. Seismol. Soc. Am.* **95**, 1412-1427.

- Day, S. M., Bielak, J., Dreger, D., Graves, R., Larsen, S., Olsen, K. B., Pitarka, A., and Ramirez-Guzman, L., 2006. Numerical simulation of basin effects on long-period ground motion, *Proceedings of the 8th National Conference on Earthquake Engineering*, April 18–22, San Francisco, California, paper No. 1857.
- Day, S. M., Graves, R., Bielak, J., Dreger, D., Larsen, S., Olsen, K. B., Pitarka, A., and Ramirez-Guzman, L., 2008. Model for basin effects on long-period response spectra in southern California, *Earthquake Spectra* **24**, 257–277.
- Erickson, D., McNamara, D. E., and Benz, H. M., 2004. Frequency-dependent Lg Q within the continental United States, *Bull. Seismol. Soc. Am.* **94**, 1630–1643.
- Field, E. H., 2000. A modified ground motion attenuation relationship for southern California that accounts for detailed site classification and a basin depth effect, *Bull. Seismol. Soc. Am.* **90**, S209–S221.
- Frankel, A., McGarr, A., Bicknell, J., Mori, J., Seeber, L., and Cranswick, E., 1990. Attenuation of high-frequency shear waves in the crust, measurements from New York State, South Africa, and southern California, *J. Geophys. Res.* **95**, 17,441–17,457.
- Geomatrix Consultants, 1995. *Seismic Design Mapping State of Oregon*, report prepared for the Oregon Department of Transportation, Personal Services Contract 11688, Geomatrix Consultants Project No. 2442, January.
- Graves, R. W., 1994. *Simulating the 3D Basin Response in the Portland and Puget Sound Regions from Large Subduction Zone Earthquakes*, USGS Award 1434–93-G-2327, Annual Technical Report.
- Idriss, I. M., 1991. *Procedures for Selecting Earthquake Ground Motions at Rock Sites*, National Institute of Standards and Technology, Report No. NIST GCR 93–625.
- Joyner, W. B., 2000. Strong motion from surface waves in deep sedimentary basins, *Bull. Seismol. Soc. Am.* **90**, S95–S112.
- Magistrale, H., Day, S. M., Clayton, R., and Graves, R. W., 2000. The SCEC southern California reference three-dimensional seismic velocity model version 2, *Bull. Seismol. Soc. Am.* **90**, S65–S76.
- Oppenheimer, D., Beroza, G., Carver, G. et al., 1993. The Cape Mendocino, California Earthquakes of April 1992: Subduction at the Triple Junction, *Science* **261**, 433–438.
- Pinheiro, J., and Bates, D., 2000. *Mixed Effects Models in S and S-PLUS*, Springer, New York, NY, 528 pp.
- R Development Core Team, 2006. *R: A Language and Environment for Statistical Computing*, R Foundation for Statistical Computing, Vienna, Austria. ISBN 3–900051–07–0, <http://www.R-project.org>.
- Raoof, M., Herrmann, R., and Malagnini, L., 1999. Attenuation and excitation of three-component ground motion in southern California, *Bull. Seismol. Soc. Am.* **89**, 888–902.
- Sadigh, K., Chang, C.-Y., Egan, J. A., Makdisi, F. I., and Youngs, R. R., 1997. Attenuation relationships for shallow crustal earthquakes based on California strong motion data, *Seismol. Res. Lett.* **68** (1), 180–189.
- Sibson, R. H., and Xie, G., 1998. Dip range for intracontinental reverse fault ruptures: Truth not stranger than friction, *Bull. Seismol. Soc. Am.* **88**, 1014–1022.
- Silva, W. C., Abrahamson, N., Toro, G., and Costantino, C., 1996. *Description and Validation of the Stochastic Ground Motion Model*, report submitted to Brookhaven National Laboratory, Associated Universities, Inc., New York (available at www.pacificengineering.org).

- Somerville, P., Collins, N., Graves, R., Pitarka, A., Silva, W., and Zeng, Y., 2006. Simulation of ground motion scaling characteristics for the NGA-E project, *Proceedings of the 8th National Conference on Earthquake Engineering*, April 18–22, San Francisco, California, paper No. 1789.
- Somerville, P. G., and Abrahamson, N. A., 1995. *Prediction of Ground Motions for Thrust Earthquakes*, Report to the California Strong Motion Instrumentation Program (CSMIP).
- Spudich, P., Joyner, W. B., Lindh, A. G., Boore, D. M., Margaris, B. M., and Fletcher, J. B., 1999. SEA99: A revised ground motion prediction relation for use in extensional tectonic regimes, *Bull. Seismol. Soc. Am.* **89**, 1156–1170.
- Toro, G. R., 1981. Biases in Seismic Ground Motion Prediction, Ph.D. Thesis, Dept. of Civil Eng., Massachusetts Inst. of Technology, 133 pp.
- Walling, M., Silva, W., and Abrahamson, N. A., 2008. Non-linear site amplification factors for constraining the NGA models, *Earthquake Spectra* **24**, 243–255.
- Wills, C. J., and Clahan, L. B., 2006. Developing a map of geologically defined site-condition categories for California, *Bull. Seismol. Soc. Am.* **96** (4A), 1483–1501.
- Youngs, R. R., 1993. Soil amplification and vertical to horizontal ratios for analysis of strong motion data from active tectonic regions, Appendix 2C in *Guidelines for Determining Design Basis Ground Motions, Vol. 2: Appendices for Ground Motion Estimation*, EPRI Report TR-102293.
- Youngs, R. R., Abrahamson, N., Makdisi, F., and Sadigh, K., 1995. Magnitude Dependent Variance of Peak Ground Acceleration, *Bull. Seismol. Soc. Am.* **85**, 1161–1176.

(Received 30 July 2007; accepted 25 January 2008)